FLIGHT AND SYMBOLIC MODELING OF A 3D PRINTED ORNITHOPTER

A Thesis

Presented to the Faculty of the Graduate School

of Cornell University

in Partial Fulfillment of the Requirements for the Degree of

Master of Science

by

Charles Richter

January 2012

ABSTRACT

The work described in this thesis represents a set of novel solutions to several challenges involved in the design and flight of hovering ornithopters as well as the measurement and analysis of lift forces produced by wings flapping in air. First, a method was developed to 3D print functional flapping wings. The use of 3D printing technology has greatly expanded the possibilities for wing fabrication, allowing wing shapes and structures to replicate those of real insects or virtually any other design. It has also reduced the time required for wing fabrication to under one hour. A passively stable hovering ornithopter with a mass of 3.89 grams was constructed using the 3D printing technique and was flown for 85 seconds. This flight demonstrates the functional utility of printed materials in the construction of flapping wings and ornithopters, which are important experimental capabilities for understanding the principles of insect flight and control. 3D printed wings were then used to conduct aerodynamic experiments and an apparatus was constructed to measure the instantaneous lift forces produced by flapping wings at the scale of those used in micro air vehicles, with Reynolds numbers in the range 2500-5000. Custom software was written to extract the three dimensional kinematics of flapping from high-speed video recorded during each experiment. Finally, the experimental data were analyzed to measure the accuracy of several quasi-steady lift force equations from the literature, and additional models were developed using a data-mining process based on the Eureqa symbolic regression software. The models developed by Eureqa were more accurate than analytical equations and were much simpler, as measured by equation size. Furthermore, Eureqa automatically separated the experimen-

tal data into sums of distinct terms with understandable physical significance, such as translational aerodynamic lift and inertial forces, with no prior knowledge of the structure of the system. This result suggests that Eureqa could be used to lend insight in parsing the primary dynamic components in a wide variety of complex systems.

BIOGRAPHICAL SKETCH

Charlie Richter grew up in the Chicago suburb of River Forest, Illinois. He was drawn to science and engineering from an early age, developing his mechanical skills through constant projects. Beginning with Legos and Erector Set, Charlie moved on to more ambitious goals and built numerous radio-controlled model vehicles, tree houses, and a go-kart among many other engineering endeavors. Meanwhile, he also played a range of musical instruments including violin, trumpet, trombone and guitar. Eventually, he merged his interests in music and engineering by teaching himself the art of lutherie and building two electric guitars. Charlie was also an athlete, playing ice hockey on his high school team and racing sailboats on Lake Michigan. Upon graduating from Oak Park and River Forest High school in 2003, he followed his dreams of flight and earned his Private Pilot Certificate. Charlie then enrolled at Cornell University, where he explored his broad academic interests including engineering, science and humanities. He was a member of the Cornell Sailing Team all four years of his undergraduate career, and served for two years as Captain of the team. Charlie graduated with a Bachelor of Arts degree in government in 2007, but soon his love of engineering took hold once more and he completed a Bachelor of Engineering degree at Dartmouth College in 2009 before returning to the Sibley School of Mechanical and Aerospace Engineering at Cornell for graduate studies.

This thesis is dedicated to my parents, Susan and Harry.

ACKNOWLEDGEMENTS

First and foremost I would like to thank my advisor, Hod Lipson, for fostering a creative and energetic research atmosphere and for sharing his wisdom and encouragement as I explored uncharted territory in my work. I am grateful to the members of the Creative Machines Lab for creating such a fun environment. I feel fortunate to have been a part of this very special place for invention and research. I would like to thank Professor Itai Cohen, who provided inspiration for my research project and contributed to its success by sharing his expertise in insect flight. I am also grateful to Professors Charles Williamson and Mark Campbell for their advice and encouragement along my academic path.

I owe a very special thanks to my friends at Cornell and my housemates at the Gamma Alpha co-op for making these years so much fun. It was their companionship and persistent pursuit of adventure that produced so many wonderful memories. Finally, I would like to thank my parents for their constant support in my studies and for nurturing my lifelong love of building.

TABLE OF CONTENTS

LIST OF TABLES

LIST OF FIGURES

CHAPTER 1

INTRODUCTION

Hovering flapping flight of insects and birds has long fascinated scientists and engineers, but only in the last decade has it been successfully demonstrated by man-made flying machines. Designing and constructing a hovering ornithopter poses several unique challenges that are not encountered with conventional aircraft. First, the aerodynamics of flappling lift production is different from fixed wing and rotary wing aircraft because of the high angles of attack, rapid accelerations of the wing, dynamic stall and unsteady effects of vorticity. Second, the dynamics of a hovering ornithopter are difficult to control. Hovering flapping vehicles and insects often exhibit fast instabilities in pitch and roll directions, which must be stabilized through active or passive means, often without the aid of conventional control surfaces such as those used in airplanes. Therefore, in the most sophisticated ornithopters that mimic insects, control is achieved by modulating the wing kinematics, which requires a significant increase in mechanical complexity, weight and sensing ability. Furthermore, the dynamics of a single flapping wing is itself a very complex system. Most ornithopters allow the wings to passively rotate to the optimal angles of attack during flapping, but this passive rotation is a combination of inertial and aerodynamic forces and is highly sensitive to the wing shape and distribution of area, complicating the design process of optimizing an ornithopter wing. Finally, engineering materials and power solutions have only recently been improved to enable flapping hovering flight of man-made ornithopters in the past decade. Standard DC motors have often been used even though rotational motion is not well suited to the reciprocating motion of a flapping wing, however linear actuators such as piezoelectric devices lack the necessary strength and require electrical power

solutions far exceeding what can be practically carried onboard an ornithopter. The materials used in ornithopter construction and testing are often lightweight but fragile, such as balsa wood and tissue paper, or require a sophisticated and delicate fabrication process, such as carbon fiber and mylar. Neither of these options lend themselves to quickly producing many high-precision specimens for aerodynamic testing, so new methods are needed.

This thesis presents a collection of work aimed at solving several of challenges of design, fabrication and testing of ornithopters. First, a method of 3D printing flapping wings was developed, featuring precise control over the geometric and structural parameters needed to obtain the desired dynamic behavior and passive wing rotation required for lift production during flapping. Next, a 3D printed ornithopter was designed, built and flown to demonstrate the functionality of 3D printed wings and other functional 3D printed parts. This design process motivated a study of the aerodynamics of flapping wings, using 3D printing to create test specimens and using a data-driven approach to modeling their behavior, with the aim of optimizing wing designs based on the resulting models. An experimental apparatus was developed with accompanying software to measure the kinematics and instantaneous lift forces produced by flapping wings. This apparatus was used to collect data from eleven different wing designs, each flapping at five different speeds and three different flapping amplitudes over a range of Reynolds numbers between 2500 and 5000. The data collected from these experiments was used to evaluate a variety of quasi-steady analytical models from the literature and to develop new equations using a data-mining process enabled by the Eureqa symbolic regression software. While the analytical models provided an accurate prediction of forces produced by flapping wings, they required complex calculations involving wing geom-

etry and flapping kinematics. In contrast, the equations developed by Eureqa were much simpler than analytical models and were simultaneously more accurate. This thesis describes the process and results of each stage of this research: Design, construction and flight of a 3D printed ornithopter, development of an experimental apparatus to measure the instantaneous lift force produced by a flapping wing, and the process of data mining used to obtain symbolic models of the equations with a comparison of existing quasi-steady aerodynamic equations from the literature.

CHAPTER 2

UNTETHERED HOVERING FLAPPING FLIGHT OF A 3D PRINTED ORNITHOPTER

2.1 Introduction and Review of Existing Work

Unlike forward flight, hovering flapping flight poses several special challenges. First, the theoretical and experimental work on the complex aerodynamics of flapping wing flight is not as developed as it is for the aerodynamics of conventional aircraft. Second, the natural dynamics of hovering flapping flight is generally unstable and requires a sophisticated solution to maintain an upright flying position [39, 38]. Third, the energy density of batteries was insufficient for the power demands of hovering flight until small lithium-based batteries became widely available. However with the improvement of electrical power solutions, a number of successful hovering ornithopters have been developed with a variety of wing designs. This project utilizes existing solutions to the power and stability problems and uses 3D printing as a novel approach to designing and manufacturing the fuselage and the wings (Fig. 2.1).

Thus far, producing effective flapping wings for research and ornithopter construction has been a time consuming and delicate process taking hours or days to complete. The 3D printing technique allows wings to be produced in a matter of minutes, dramatically reducing the time of each design cycle. Overcoming this barrier to experimentation will allow a comprehensive study of lift production for a wide variety of wing shapes including those replicating real insect wings.

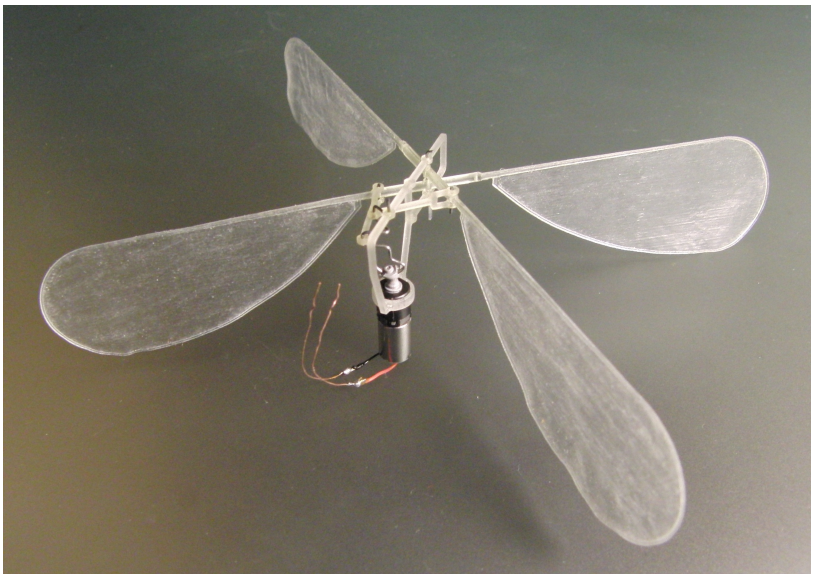

Figure 2.1: 3D-Printed ornithopter.

A comprehensive understanding of flapping wing aerodynamics and hovering flight will become increasingly important as ornithopters shrink to the scale of real insects where some advantages of flapping wing flight are realized [15]. These advantages include efficiency and maneuverability improvements over fixed and rotary wing aircraft at low Reynolds numbers. Furthermore, micro-scale actuators such as piezoelectric devices are naturally suited to producing the reciprocating motions of flapping, whereas larger conventional DC motors require a crank and connecting rod to convert rotary motion into linear motion [27, 47]. Maneuverable, low-power micro air vehicles have a wide range of applications including mapping, surveillance and search-and-rescue operations where small size and the ability to navigate in tight spaces are vital, or in thin extraterrestrial atmospheres where Reynolds numbers of flight may be lower than they would be on Earth [25]. Micro air vehicles also present a challenging synthesis of many areas of engineering, including materials, actuators, electronics, control, vision, guidance, and others [18, 22]. This project has demonstrated

the viability of 3D printed aerodynamic components for experimentation and for use in a real ornithopter at the scale of the smallest current designs.

The existing work that has influenced this project includes a variety of successful ornithopter designs and some research on the dynamics and control of insect flight (Table 2.1). This project is a continuation of an earlier ornithopter design project by Floris van Breugel of the Cornell Creative Machines Lab. Van Breugel's design used four motors to drive eight wings and featured passively stable flight dynamics using a set of damping sails above and below the body of the aircraft. This model had a mass of 24 g and demonstrated a stable hovering flight of over 30 seconds in 2007. Broad goals for the current project were to achieve a comparable flight time using this system of passive stability in a vehicle under 10 g.

Several other successful designs currently exist, including the series of DelFly ornithopters, which are radio controlled using tail configurations resembling fixed-wing aircraft and the AeroVironment Nano Air Vehicle, which achieves control using active wing control. The Harvard Microrobotics Laboratory has also produced ornithopters weighing 60 mg using piezoelectric actuators and insect-like passive wing pitching, but require a tether for power and stability.

Design	**Year**	**Mass (g)**	**Span (cm)**	**Wings**	**Hover (s)**	**Features**
Mentor [50]	2002	580	36	4	> 60	Nitromethane Fuel
DelFly II [10]	2006	16.07	28	4	480	Camera, R/C
van Breugel [40]	2007	24.2	45	8	33	Passively Stable
Chronister [8]	2007	3.3	15	4	unknown	R/C
Wood [46]	2007	0.060	3	2	N/A	Piezoelectric Power
DelFly Micro [10]	2008	3.07	10	4	N/A	Camera, R/C
NAV [1]	2009	10 (est.)	7.5 (est.)	2	20	Active Wing Pitching
Richter [29]	2010	3.89	14.4	4	85	3D Printed Parts

Table 2.1: Characteristics of existing ornithopter designs.

There have also been recent developments in the understanding of wing rotation in insect flight [6, 11, 43]. These studies have explored one mechanism of passive wing deflection in insect flight that is essential to the simplicity of some ornithopter designs. They have shown that some insect wings deflect to an angle of attack of 45°, which is thought to be optimal for lift production of a flat plate wing. Related studies have also given rise to hypotheses explaining forward thrust, flight maneuvers and disturbance rejection, and experiments could be designed to examine these hypotheses using the ornithopter as a test bed [32, 30, 31, 5, 12].

2.2 Motivation and 3D Printing

One primary goal of this project was to produce a hovering ornithopter with as many 3D printed components as possible. An Objet EDEN260V printer and the Objet FullCure 720 material were used to produce all printed components. The cost of the material was roughly 0.22 USD per gram and the EDEN 260V printed with a resolution of 42 μm on the x-and y-axes and 16 μm on the z-axis. At first, only the fuselage, hinges and pushrods were printed, however a method of printing entire one-piece wings was soon developed.

First attempts at wing construction were aimed at recreating the wings of the van Breugel design, using a carbon fiber rod as the main strut, polyethylene terephthalate (PET) stiffening ribs and a Mylar film wing surface. The carbon fiber rod was to extend out of a 3D printed hinge, but after several design iterations, the hinge, strut and stiffening ribs were combined into a single printed piece. When further experimentation revealed that a durable thin film could be

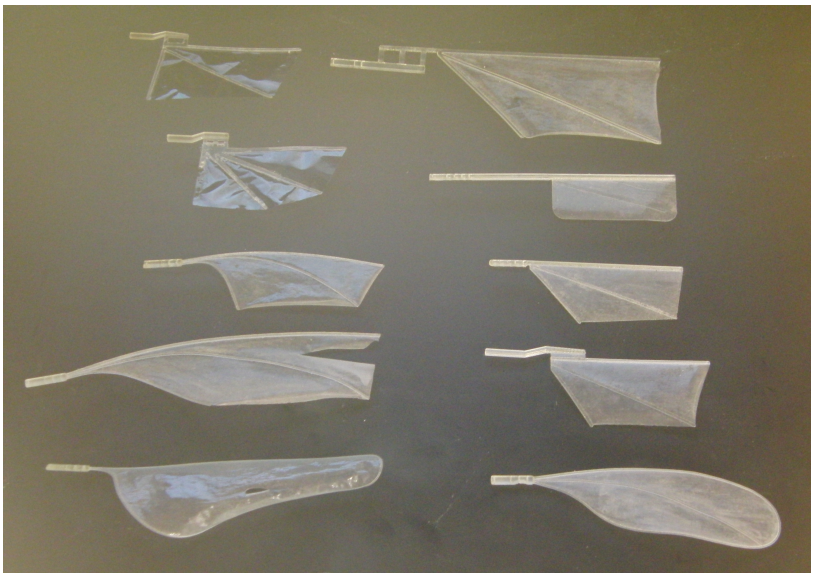

Figure 2.2: Wings with 3D printed frames and glued Mylar film (upper left), biologically inspired shapes (lower left) and designs with stiffening ribs (right).

printed using only two layers of printed material, this film was used instead of Mylar as the wing surface and the first one-piece printed wings were made. Fig. 2.2 shows many conventional and biologically inspired designs.

2.3 Printed Wing Construction

The printed wings of the ornithopter were composed of three functional elements: the central beam, the surrounding frame, and the thin film wing surface. Fig. 2.3 shows the parts of the dual-wing used in the full ornithopter design.

The central beam was the most rigid portion of the wing and contained the pivot point as well as the attachment holes for the connecting rods. While other designs require a bushing or dedicated hinge, 3D printing allowed the hinge to be incorporated into the main beam design. Furthermore, the FullCure 720

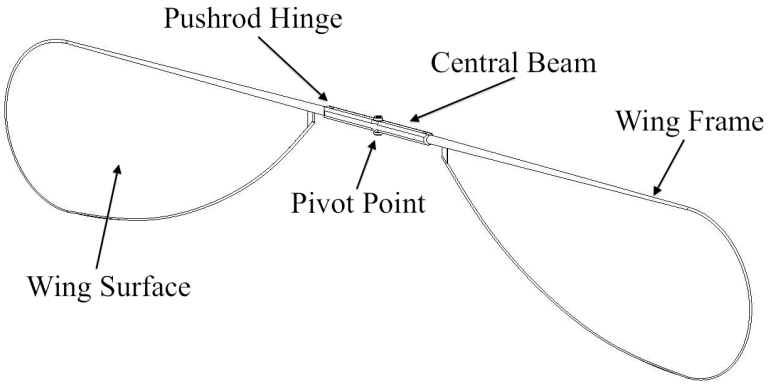

Figure 2.3: Parts of the one-piece printed wing.

material featured relatively low friction against the stainless steel 0.5 mm piano wire hinge pins when lubricated with a drop of medium-viscosity oil. The holes for the pivot points were designed with a 0.6 mm diameter to provide an adequate gap for low-friction operation. This technique eliminated the need for a heavy bushing or complex assembly.

The outer frames of the wings were attached to the ends of the beam. The outer frames determined the flexibility of the wings and the deflection properties during flapping. The outer frames were defined in the CAD model as lofted curves connecting circular cross sections. By varying the radius of the circular cross sections at various points along the frame, the overall stiffness and flexibility patterns of the wing could be tuned.

The thin wing surface was a flexible film that extended through the area inside the outer frame. The surface had a thickness of 32 μm, which was composed of two layers of printed material. The ability of the printer to print such a thin flexible film was the development that made a one-piece printed wing possible. While it was possible to print a thinner film using a single layer, wings constructed with a single layer surface were extremely delicate and tore under the

stresses of vigorous flapping. Chamfers were used to counter the tendency of the wing film to tear at points of discontinuous geometry, such as the interface between the wing film and the outer frame.

One practical element of 3D printing technology was the use of a gelatinous material to support the structure during printing. Therefore, removing the support material was an important step in the manufacturing process, especially with delicate features such as the thin wing surface. Common methods used to remove support material included dissolving it in sodium hydroxide and spraying it off with pressurized water. However, both of these methods had limitations due to the delicacy of the thin film. When a printed wing was soaked in liquid for any period of time, it tended to curl up or become warped, which could be partially corrected by pressing it flat and allowing it to dry. However, the moisture often left some permanent warping of the wing shape. The method of spraying pressurized water was also difficult due to its tendency to tear the wing film. The most successful method of removing support material was to manually scrape it from the wing surface with a dull blade, and then to remove any remaining material by dissolving it with a cloth moistened with rubbing alcohol.

2.4 Wing Design

At the beginning of the project, the wing design process focused on narrowing the vast design space to an approximate wing size that was appropriate for the motors available and desired weight of the vehicle. During initial testing, key wing design features were identified that helped produce the appropriate

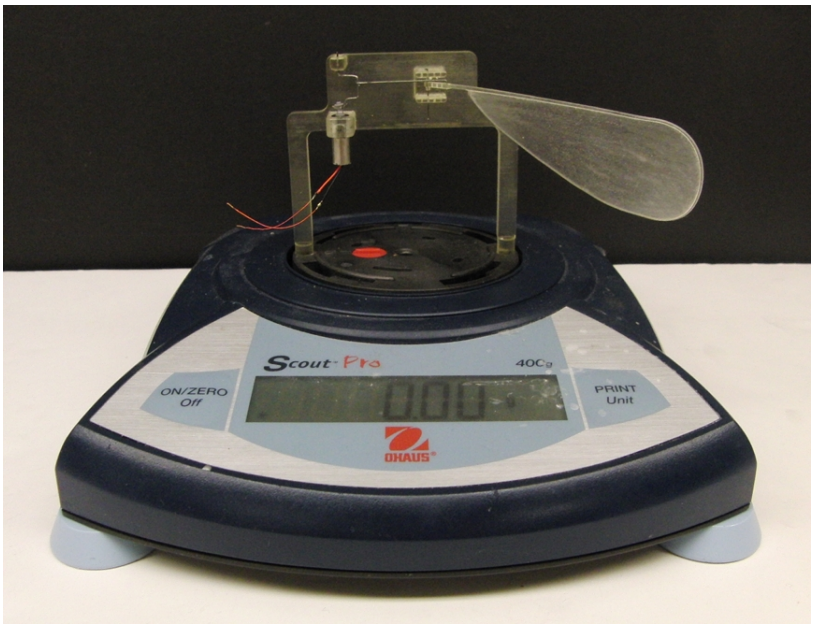

Figure 2.4: Lab scale test setup. Wing is shown upright in this picture, but was mounted upside down during experiments to prevent downwash effects.

shapes and deflections when flapping. Testing of a wide variety of wing shapes, sizes and structures was carried out by powering them with a small DC gear-motor using a DC power source. The lift of each wing was measured using a custom attachment for a digital lab scale and the flapping behavior was analyzed using a high-speed camera capturing 1000 frames per second. Fig. 2.4 and Fig. 2.5 show the experimental apparatus.

The wing size partially determined several important variables, including mass and surface area, which in turn determined how fast the wings could flap for a given power input. For the motor chosen for this project (GM 15 gear-motor available from Solarbotics.com with 25:1 gear reduction) and the power expected from a pair of Lithium-Polymer batteries (7.4V , 200mA), the best performing single wing of all wing designs tested had a length of 80 mm and a maximum chord of 30 mm. The overall weight of the wing was approximately

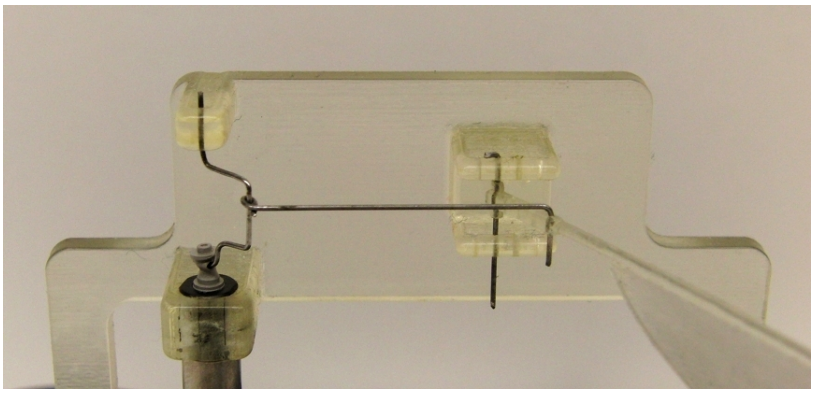

Figure 2.5: Close-up of the test mechanism.

Figure 2.6: Final wing design, chosen for its flat-plate shape during deflection to angles of attack near 45° during flapping.

0.3 g and the thickness of the wing film was 32 μm. This wing flapped at approximately 30 Hz through an angle of 110° and produced a maximum lift force of 2.92 g. This wing design is shown in Fig. 2.6.

The wing structure was important to proper deflection and wing shape during flapping. For maximum lift, the wing was designed to deflect to an angle of attack of roughly 45° at mid-stroke. This angle of attack could be tuned by adjusting the stiffness of the main wing strut. One major problem associated with early passively-deflecting wing designs was that they did not deflect as flat plates. Instead, the leading edge tended to remain vertical rather than flexing torsionally, while the wing surface bent away underneath it, resulting in an

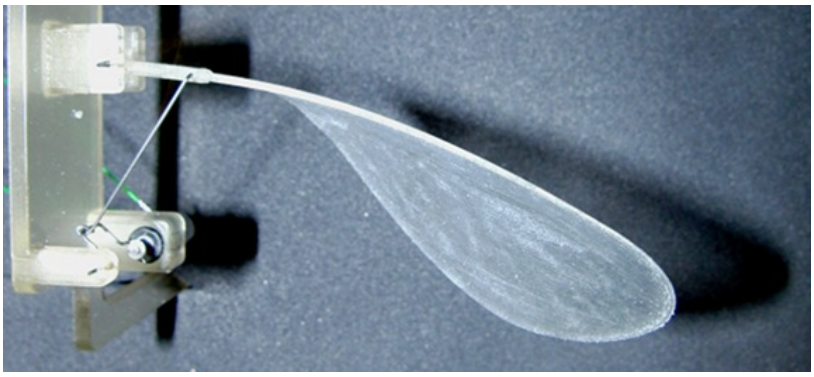

Figure 2.7: Top-down view of the final wing design flapping on the test stand, showing wing deflection.

undesirable inverse-camber shape. Several methods were explored to overcome this problem. The most effective solution was to extend the wing frame all the way around the tip of the wing. This design forced the leading edge to twist when the wing deflected, thus maintaining a roughly continuous slope across the chord of the wing near the tip. In other words, the tip of the wing behaved more like a flat plate with the entire wing deflecting to the proper angle, rather than just the lower half.

Wing ribs were also been used to control the deflection patterns and add stiffness in certain directions. Various rib designs were tested, featuring rectilinear patterns as well as curved patterns inspired by the wings of dragonflies and other insects. However, the final design did not feature stiffening ribs. Fig. 2.7 shows a top-down view of the final wing design without stiffening ribs deflecting during flapping tests on the experimental setup. This general wing design, while not necessarily optimal, was deemed satisfactory for use in the challenge of building a full ornithopter using 3D printed wings. A new double-ended version of this wing shape was produced for use in the full ornithopter.

2.5 Full Ornithopter Design

Once a satisfactory wing design was obtained, it was implemented in the four-wing vehicle. The wing chosen for this purpose was the rib-less design that produced the greatest lift. A fuselage was designed to hold the motor, crank, and wing hinge. Care was taken to place the motor as close as possible to the wing pivot point in order to position the center of mass near the center of lift.

The wings were driven by a crankshaft connected to the motor's gearbox. In order to drive the wings in a roughly symmetrical motion, the crankshaft included two attachment points for the connecting rods powering the left and right wing. These two attachment points were positioned roughly 30° out of phase from each other to compensate for the asymmetry of the crank position with respect to the left and right wings. This offset-crank mechanism can be seen in Fig. 2.8, and is similar to the DelFly I design [9] and many toy ornithopters.

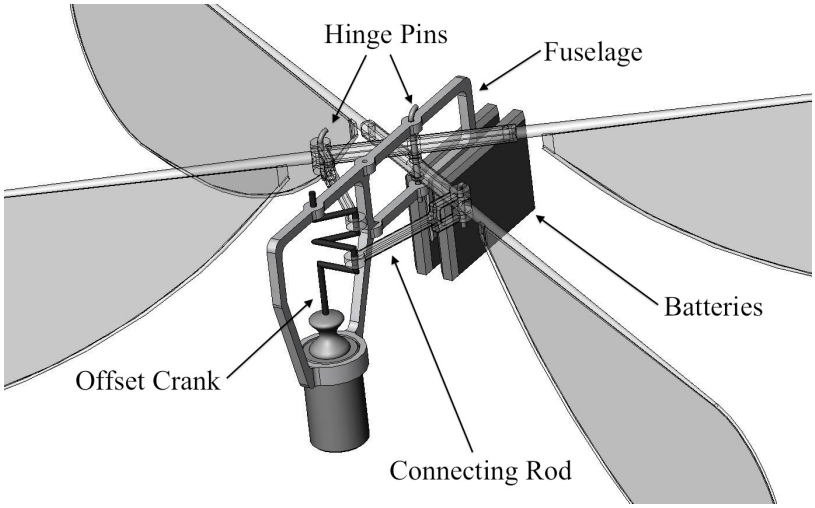

Figure 2.8: CAD model of mechanism showing offset crank and connecting rods to drive the wings.

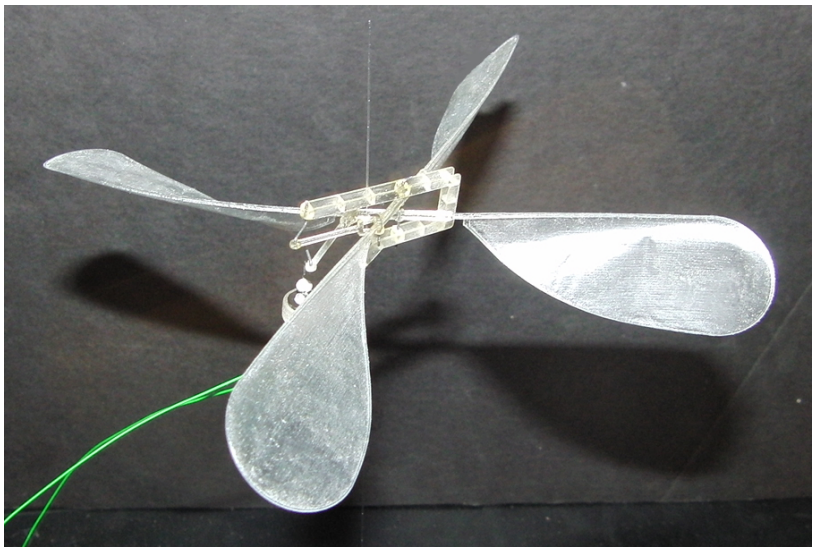

Figure 2.9: Flash photo showing wing deflection in a tethered flight test.

The ornithopter was first tested using a tether for stability and off-board power from a DC power source to verify proper operation of the crank mechanism and proper flapping behavior of the wings. The crank was designed to flap each of the four wings through an angle of roughly 80°. Given the bending in the wings at stroke reversal, this angle was enough to allow opposing pairs of wings to come into contact in a 'clap and fling' motion at the end of each stroke. The clap and fling phenomenon may aid in lift production [24]. Fig. 2.9 shows a photo of a tethered flight test showing ideal wing deflection of roughly 45°. In this test configuration, the ornithopter was able to lift up to 1.5 g of payload, which was roughly equivalent to the mass of batteries required for flight. Fig. 2.10 shows a breakdown of the total mass of the ornithopter.

Once the ornithopter was able to support a payload while flying on the tether, it was outfitted with batteries and untethered flight tests began. Two 10 mAh Lithium Polymer batteries were used to power the motor and were attached on the opposite side to the motor to balance the mass. The other feature

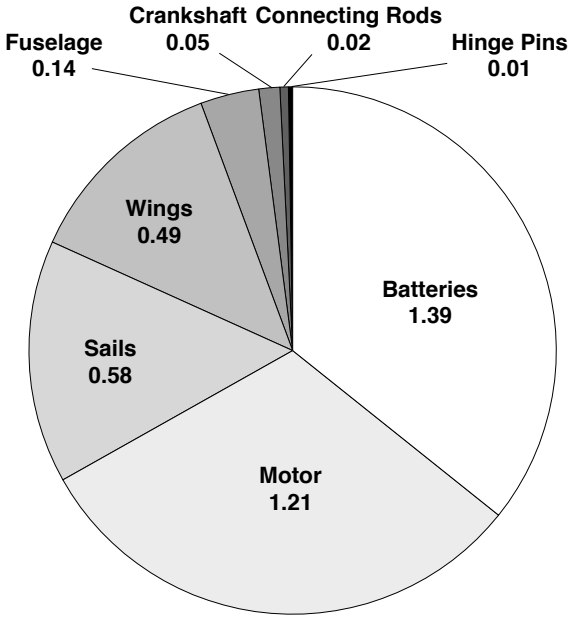

Figure 2.10: Breakdown of total mass (3.89 g).

required for untethered flight is a set of thin foam damping sails attached to a thin carbon fiber rod above and below the fuselage to maintain an upright flying position. This method of achieving passive stability was developed by van Breugel and is replicated here [40].

2.6 Passive Stability

The sails employed to maintain stability helped to keep the ornithopter upright. Without sails, or with sails that were not sufficiently large, the ornithopter entered a pattern of unstable pitching oscillations while hovering. The pitching of the ornithopter created a horizontal component of the thrust vector and therefore induced a translational motion. The upper sail provided a restoring force that opposed this translational motion and provided a righting moment, while

the lower sail damped out the swinging pendulum motion of the ornithopter below the upper sail. When launched upside down, the ornithopter righted itself, demonstrating the robustness of the design. Fig. 2.11 shows the complete ornithopter including sails.

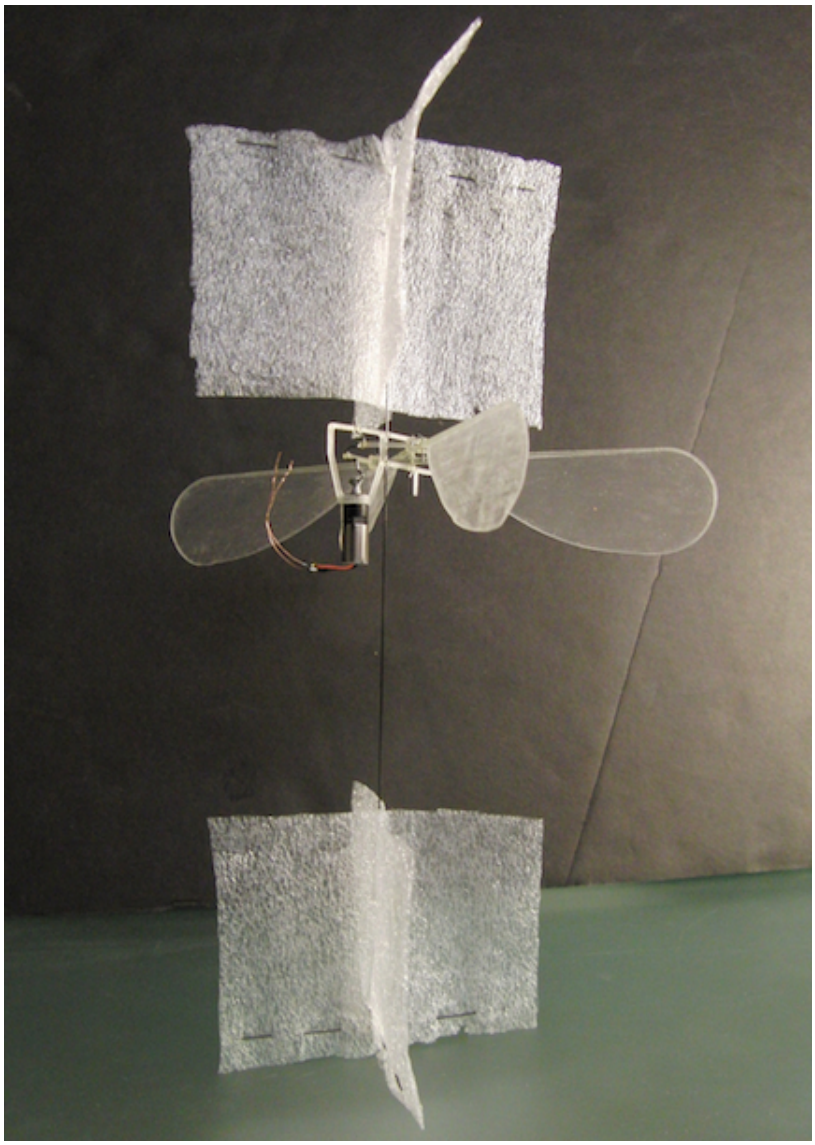

Figure 2.11: Final design with sails for passive stability.

2.7 Lift and Power Characterization

The four-wing configuration was evaluated in a series of experiments to characterize its lift and power. A test apparatus was designed to replicate the exact geometry and kinematics of the ornithopter fuselage, however a more powerful motor was selected in order to flap the wings at a steady frequency for extended periods without overheating. For this purpose, the Mabuchi FF-050 motor and BaneBots 11:1 gearbox were used. The four-wing test setup was mounted to a laboratory scale to measure average lift force and is shown in Fig. 2.12.

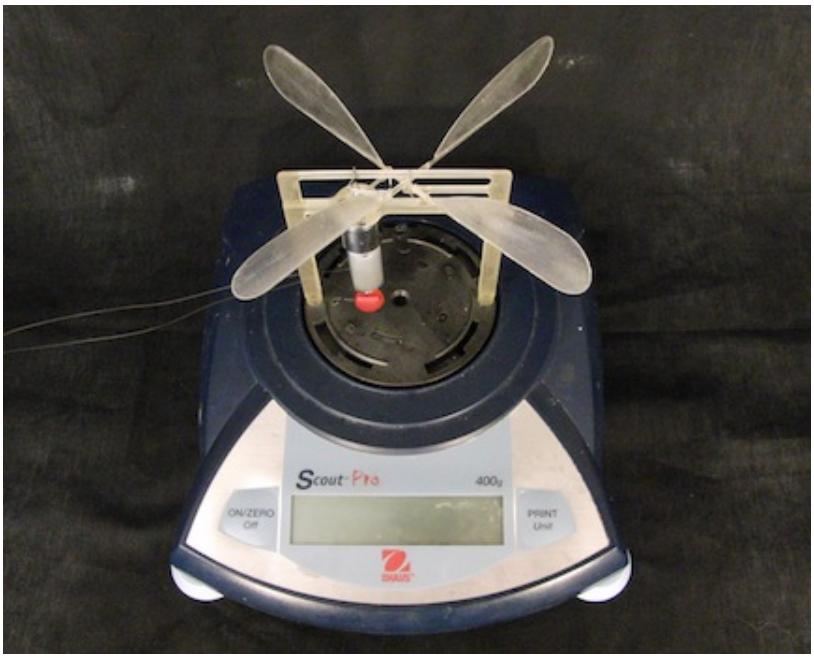

Figure 2.12: Test model for characterizing lift and power consumption of the four-winged ornithopter.

Five identical sets of wings were 3D printed and each set was tested individually. During each test, the wings were flapped at a range of speeds while voltage, current, frequency and mean lift force were recorded. Frequency was measured using a stroboscope while voltage and current were measured using

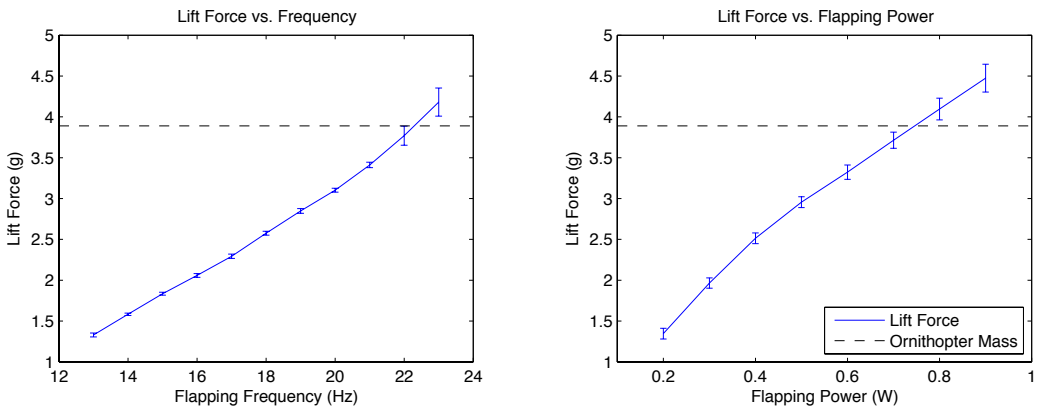

(a) (b)

Figure 2.13: Lift of the four-winged ornithopter versus flapping frequency (a), and lift versus power power supplied to the motor minus the power required to drive the linkage mechanism alone at the same frequencies (b). These plots show the average of five independent trials with error bars indicating standard deviation.

multimeters. The power required to drive the motor and linkage mechanism without wings was also recorded at a range of frequencies corresponding to the flapping tests. At each frequency, this value was subtracted from the total power consumption to give a meaningful measurement of flapping power at that frequency. This measurement represents both inertial and aerodynamic power requirements of flapping.

The plots in Fig. 2.13 show lift force as a function of frequency and flapping power. The dashed line represents the mass of the complete ornithopter, which is the lift force required for hovering. The standard deviations in these experiments, represented by the error bars in Fig. 2.13, are very small. The mean standard deviation of lift force across all frequencies of flapping in these experiments was just 1.53 percent, indicating excellent consistency among 3D printed copies of the same wing design. This consistency also reflects the precision

available for tuning the wing structure that makes 3D printing a versatile and powerful technique for wing experimentation.

2.8 Conclusions

This project yielded several significant results. First, wing tests and the hovering demonstration validated the concept of a printed ornithopter. This method of construction greatly accelerated the design cycle, enabling a set of wings to be printed in less than 30 minutes and a complete set of ornithopter parts to be printed in 60 minutes. Thus, several design iterations could be tested per day.

The Objet FullCure 720 material showed some limitations, particularly in its mechanical properties. It is not as light or as stiff as carbon fiber or balsa wood, which were the main alternative options for wing struts. Therefore, printed wings probably lost more energy to the friction involved in bending than comparable carbon fiber or balsa wood wing structures. Other limitations of the 3D printed material included a tendency of thin wings to curl up after a period of days, rendering them useless. This problem was corrected by storing wings between flat plates, but required disassembly of the ornithopter. Thin wings also developed small tears after minutes of vigorous flapping, however this problem was partially prevented with chamfered edges along the wing frame to avoid discontinuous geometry.

Experimentation with wing designs began to uncover some of the features and parameters of successful wings for this size and power scale. The GM15 motor appeared to be well matched to wings with span between 80 and 100 mm and chord length between 30 and 40 mm when running at a power 1.5

W (average power consumption during flight). Longer wing spans slowed the speed of flapping at comparable power levels, thereby reducing lift.

One very successful design feature was the wing frame that extended around the wingtip. This feature helped maintain a continuous wing slope at the tip of the wing and helped approximate the flat-plate airfoil cross section of many hovering insects. The continuous wingtip frame was a design borrowed from the structure of dragonfly wings, which exhibit ideal shape and deflection at the wingtips. Overall, the use of 3D printing to create flexible wings that were aerodynamically functional was the main accomplishment of this project and will be one area for future improvement and research.

CHAPTER 3

FLAPPING WING LIFT EXPERIMENTS

3.1 Introduction and Review of Existing work

The 3D printed ornithopter depicted in the previous chapter was designed largely through an iterative process, which converged on a wing design that produced sufficient lift given the power constraints of the chosen motor and battery. This process motivated the need for simple equations to describe the behavior of flapping wings, both to enable prediction of lift and power in future ornithopter designs as well as to enable automated optimization [28]. With this goal in mind, a set of experiments was designed to measure the lift of flapping wings as a function of their geometry and the kinematic variables of their motion. These experiments were designed to benefit from the technique of 3D printing flapping wings in order to quickly and easily produce a wide variety of wing designs with great flexibility and precise control over wing characteristics. This method would, in principle, pave the way toward examination of complex factors in flapping such as camber, twist, stiffening ribs, and other wing features that could be readily produced with a 3D printer. These experiments were also conducted with the intent of applying a data-driven symbolic modeling technique to provide simple, efficient empirical models for use in the design of future ornithopters. This component of the study features a comparison of data-driven models obtained using the Eureqa software with several analytical calculations from the literature. The purpose of this comparison is to evaluate the accuracy and complexity of various models and to examine the ability of a data-driven process to lend insight into the physics of flapping wings.

Numerous studies have measured the forces produced by a flapping wing in various experimental setups including flapping in a liquid bath such as oil [41], by tracking the kinematics of insects in flight [20, 32] and by tracking the detailed wing motions and visualizing the airflow around the wings of insects in a wind tunnel [49]. Only recently have studies directly measured the forces involved in flapping with at-scale robotic wings or actual insects in air [45, 21]. In general, measuring the forces produced by flapping wings in air is difficult because the magnitude of the forces is small, requiring custom-built capacitive or MEMS force sensors, and because the speed of flapping and prominence of inertial effects cause significant vibrations that obscure the force measurement. The experiments described here were subject to those limitations, but nevertheless succeeded in obtaining force measurements for wings at the scale of those used in micro air vehicles with an off-the-shelf force sensor and a conventional method of driving the wing with a DC motor.

3.2 Overview of the Experimental Apparatus

The apparatus used to conduct these experiments consisted of a wing-driving mechanism mounted on a vertically-oriented force sensor for measuring lift forces and a high-speed camera for recording the kinematics of the wing during flapping. Additional components included a DC power supply to power the motor driving the wing, a pair of lamps for illumination, and a mirror angled to produce a side view of the flapping wing in the camera frame. The apparatus is shown in Fig. 3.1.

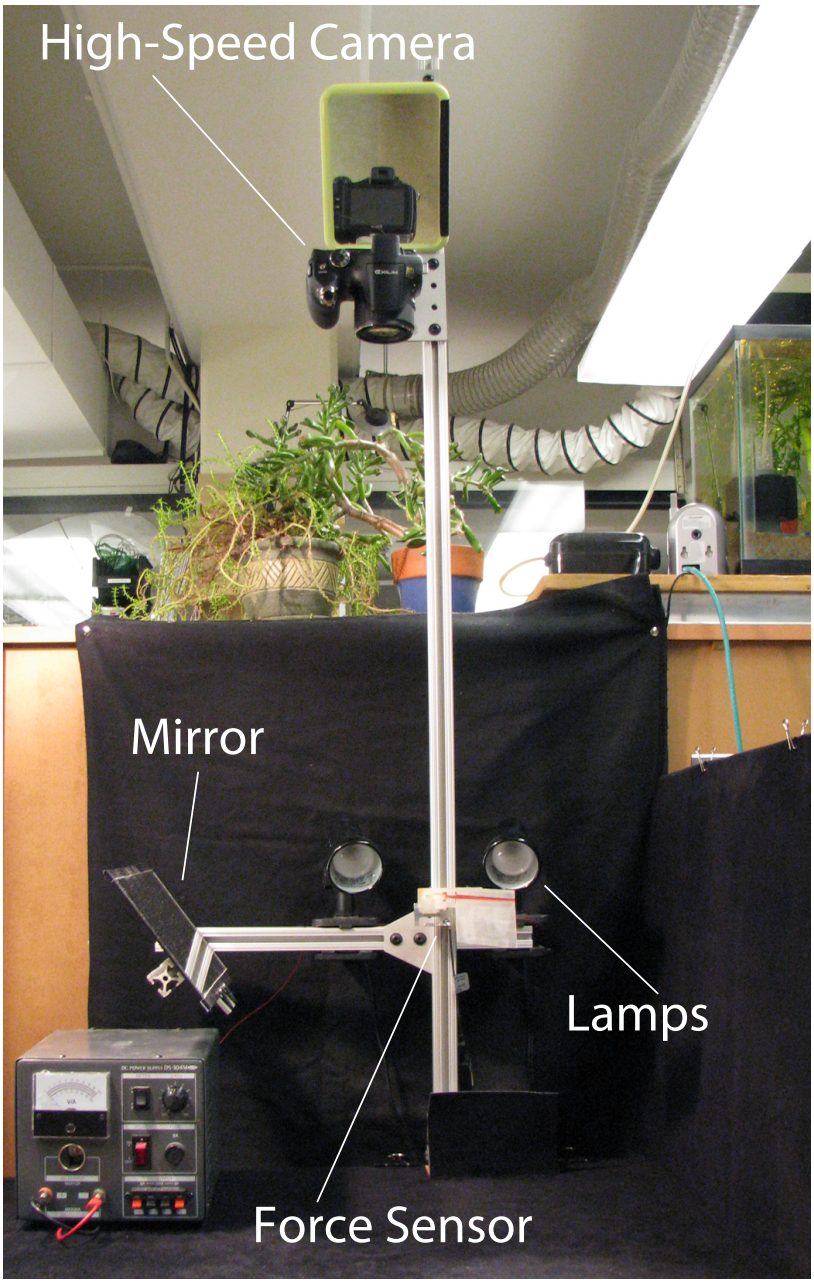

Figure 3.1: Experimental apparatus showing a wing-sensor assembly, high-speed camera, lamps, mirror and power source.

3.3 Wing-Driving Mechanism

Experimental wings were driven by a DC gear motor through a connecting rod and hand-bent wire crank, which was mated to the motor shaft using a 3D

printed shaft collar. This four-bar linkage assembly was housed within a 3D printed frame with holes that served as pivot points for the crank and wing. This frame was mounted directly to the force sensor as shown in Fig. 3.2. A detailed view of the wing-driving linkage system, including pivot points and hinge pins, is shown in Fig. 3.3.

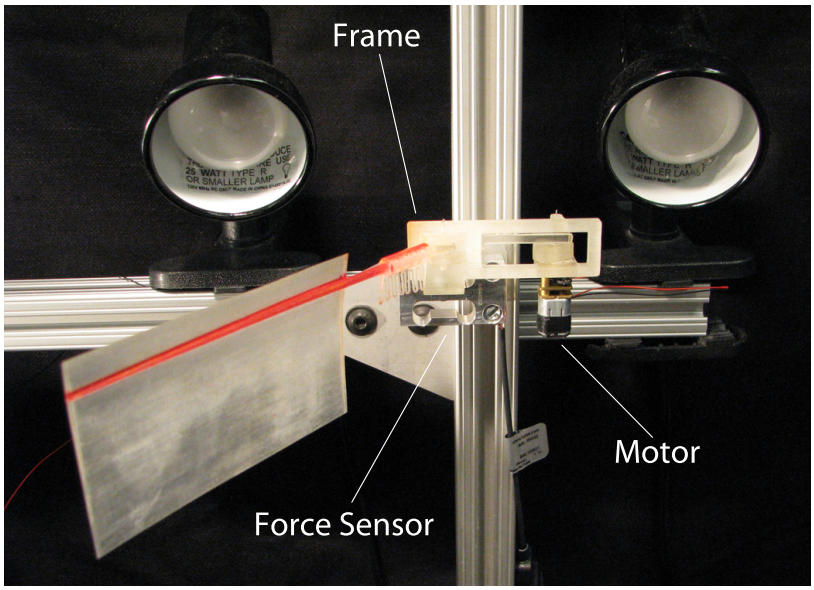

Figure 3.2: Wing-driving assembly mounted to force sensor.

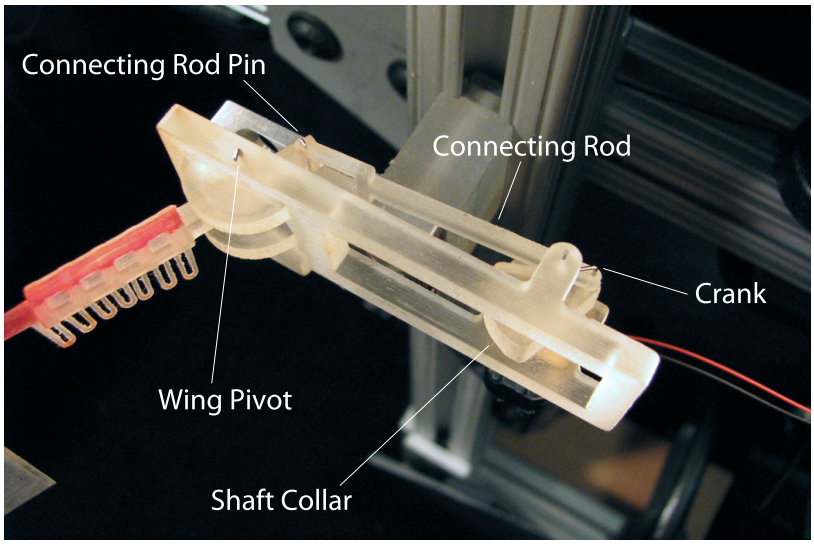

Figure 3.3: Detailed view of wing-driving mechanism and hinge pins.

3.4 Wing Design

The wings examined in this study were designed to be the simplest possible wings for examination, featuring a rectangular shape and a thin flat-plate cross-section, while being allowed to rotate passively by way of a 3D printed hinge. All wings utilized the same general structural features, including a wing root and hinge, a main strut, a pair of stiffeners and a thin film wing surface, shown in Fig. 3.4.

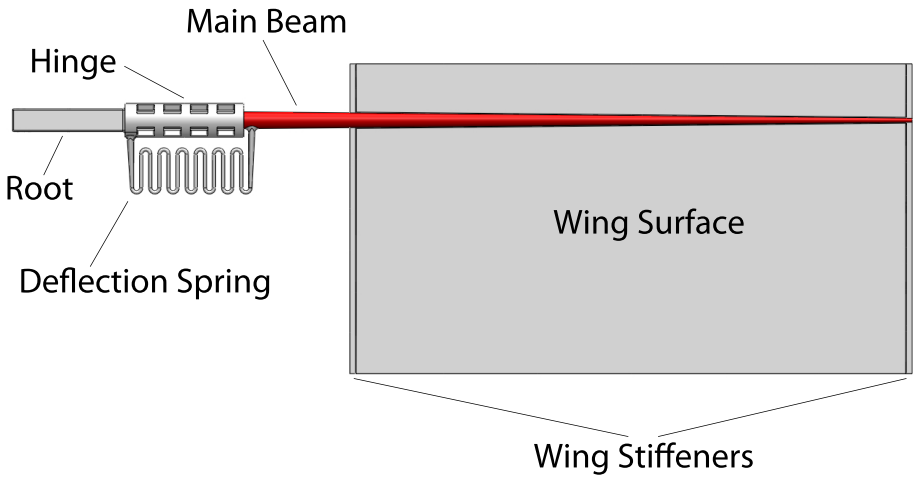

Figure 3.4: Diagram of an experimental wing, showing the root, hinge, spring, main beam, stiffeners and wing surface.

3.4.1 Wing Root

The wing root featured a pinhole through its center that served as the fulcrum for flapping, and a set of three pinholes near the end that functioned as the attachment points for the connecting rod that drove the wing. The choice of pinhole for attachment of the connecting rod allowed three different flapping amplitudes: 72°, 81°, and 96°. These pinholes of the wing root can be seen through

the translucent 3D printed material in Fig. 3.5 and the wing root is shown inserted into the frame of the flapping apparatus, attached to the connecting rod, in Fig. 3.3. The flat surfaces of the wing root were designed to slide along the semi-circular guide surfaces of the frame, constraining the wing's motion to the plane of flapping.

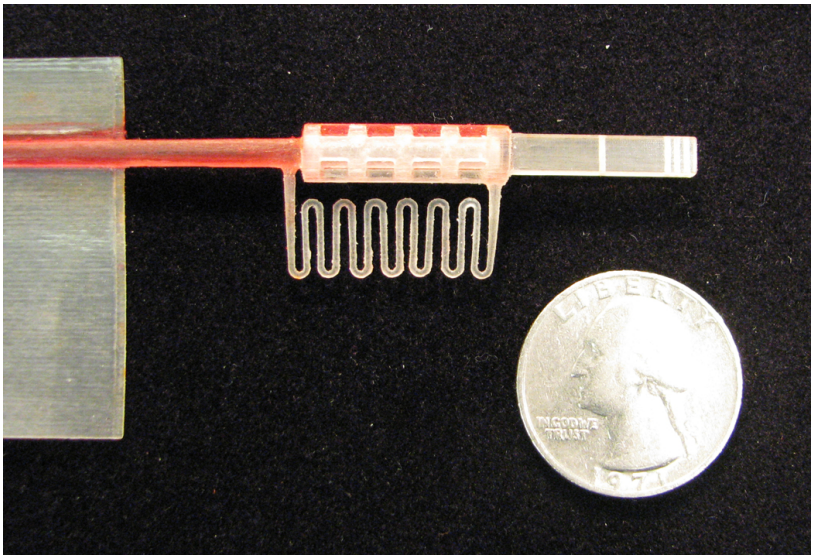

Figure 3.5: Wing root and hinge showing pinholes for flapping fulcrum and attachment of connecting rod for driving the wing.

3.4.2 Wing Hinge

Attached to the rectangular wing root was the cylindrical hinge portion of the wing structure. This hinge was critical to the function of the wing as it allowed the rigid wing surface to passively pivot back and forth about an axis along the wing span to achieve angles of attack around 45° during flapping. The hinge consisted of an outer barrel with holes, and an inner cylinder that was contiguous with the main beam of the wing and rotated inside the outer barrel when the wing rotated. The inner cylinder rested in a pair of collars with one at each

end of the outer barrel, serving as journal bearings that were lubricated with oil to minimize the friction of wing rotation. Inside the distal collar was a small lip on the inner cylinder, which locked it inside the outer barrel while still allowing it to pivot smoothly. Fig. 3.6 shows a section view of the CAD model for this hinge design. The hinge was 3D printed as a single piece with the rest of the wing, and the support material inside the outer barrel was removed during the cleaning process. The majority of support material was removed manually using a thin wire and compressed air through the holes in the outer barrel, and the remainder was dissolved with rubbing alcohol, allowing the hinge to pivot freely.

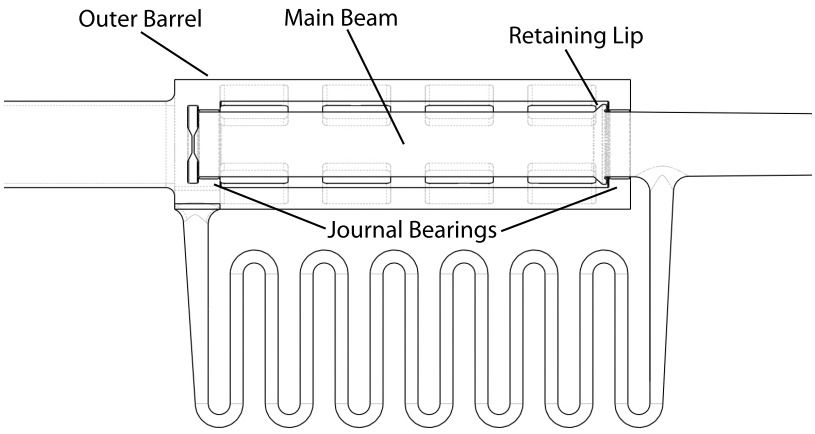

Figure 3.6: Cutaway view of wing hinge CAD model showing concentric cylinders, journal bearings, retaining lip and spring.

3.4.3 Hinge Spring

Like a real insect wings, these experimental wings were designed such that the passive deflection during flapping would be opposed by a restoring force. This

function was performed by a thin curved spring printed as part of the wing. The spring design consisted of a cylindrical member folded into 13 tight 180° curves, which can be seen in Fig. 3.6. One end of the spring was attached to the outer barrel of the hinge and the other end was attached to the main beam, thus providing a restoring force when the these two parts pivoted with respect to one another, elongating the spring.

3.4.4 Main Beam, Stiffeners and Wing Surface

The portion of the wing attached to the main beam rotated as a unit during flapping, and was intended to be essentially rigid while remaining as light as possible. The main beam was designed with a taper from a radius of 3 mm at the root to 0.8 mm at the tip, and this design provided enough rigidity to prevent spanwise bending during flapping. The stiffeners at the proximal and distal ends of the wing surface served to overcome the tendency of the thin film surface to curl or deviate from its flat-plate shape. Indeed, the wings maintained a flat profile during flapping, which simplified calculation and allowed for comparison with the existing literature on flapping aerodynamics, which has focused primarily on flat plate airfoils. The wing surface itself was designed with a thickness of 0.096 mm, which was the minimum thickness that provided the necessary stiffness to prevent deformation of the flat plate shape during flapping.

3.5 Load Cell

The load cell used in these experiments was a FUTEK model LSM250 parallelogram load cell with a USB connection for data logging. This load cell was chosen in consultation with the FUTEK application engineering staff for its combination of sensitivity and resistance to off-axis loads and moments, resulting from its geometry. Compared with other load cell geometries such as bending-beams or S-beams, the parallelogram configuration provided resistance to forces involved in flapping that were not aligned with the direction of vertical lift, most notably the high moments caused by wing accelerations at stroke reversal. Fig. 3.7 shows the load cell geometry and the strain gauges located on the bottom surface.

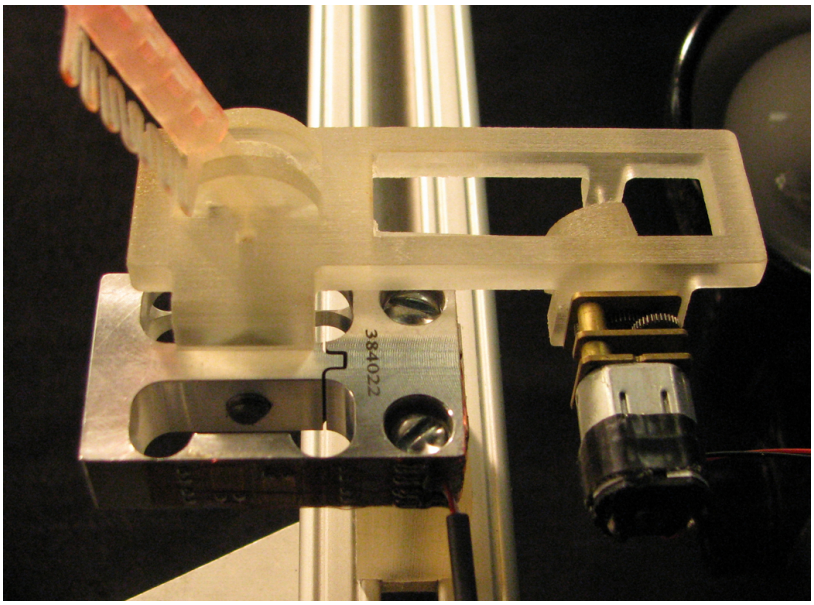

Figure 3.7: Load cell with parallelogram geometry designed to resist the off-axis forces and moments of flapping.

3.5.1 Load Cell Performance

The USB circuit used with this load cell delivered the necessary power for measurement, served as an analog-to-digital converter and interfaced with FUTEK's proprietary USB data logging software. This combination of load cell and USB connector was capable of a sampling rate of 1 kHz with a maximum available measurement precision of 10e-9 N. The advertised natural frequency of the load cell was 200 Hz, and when the mass of the wing-driving mechanism and DC motor were attached, the natural frequency of the whole apparatus was measured at approximately 70 Hz. Fig. 3.8 shows the amplitude spectrum of the force signal recorded while delivering light impulses to the apparatus, with and without a wing mounted.

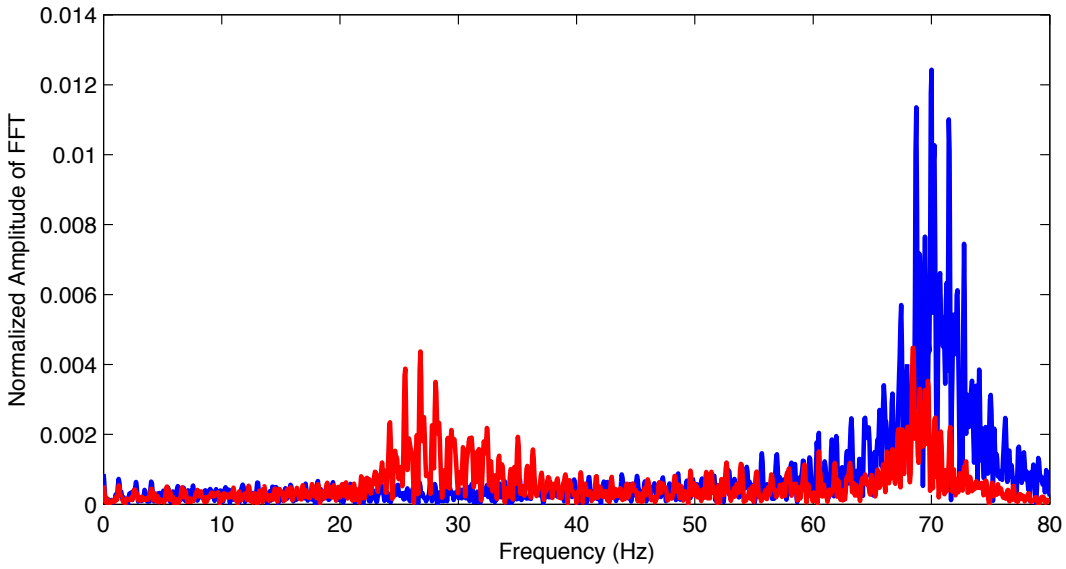

Figure 3.8: Amplitude spectrum of the force signal measured while delivering light impulses to the apparatus with a wing attached (red) and without (blue). These two amplitude spectra identify the resonant frequencies of the wing (≈26 Hz) and the wing-driving mechanism (≈70 Hz).

3.5.2 Representative Lift Force Measurement

Sample force measurements were made to characterize the output of the flapping apparatus and load cell. Fig. 3.9 shows the measured force from several periods of flapping at a frequency of 3.05 Hz along with two versions of the same measurement after high-order zero-phase lowpass-filtering with cutoff frequencies of 50 Hz and 22.9 Hz. The periodic nature of the force profile and downstroke-upstroke symmetry can be seen in the red curve, which shows the signal with a 22.9 Hz cutoff frequency. The negative peaks in the force profile are primarily an effect of the inertial forces involved in rapid wing flips near stroke reversal.

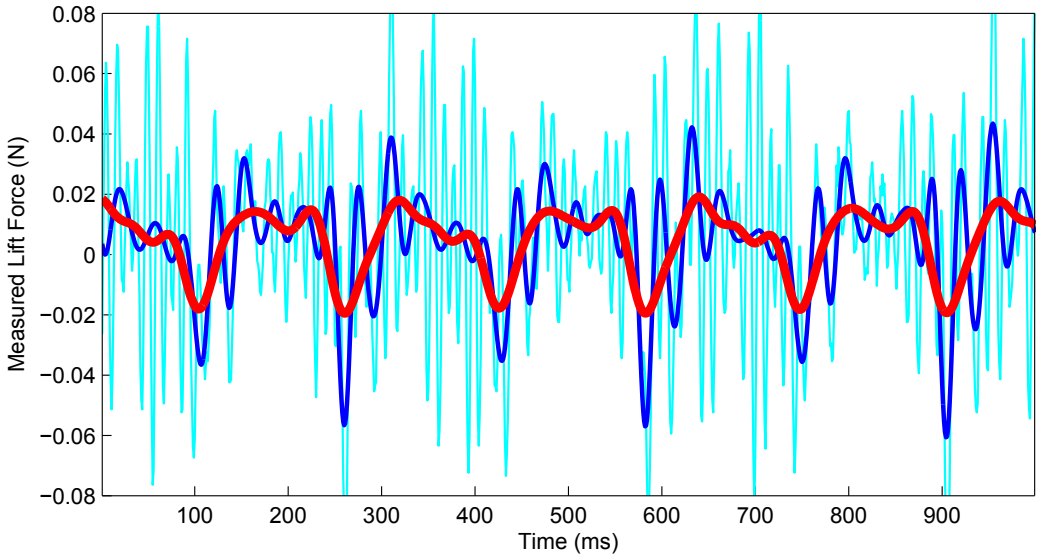

Figure 3.9: Raw force measurement from several periods of flapping at 3.05 Hz (cyan), low-pass filtered with cutoff frequencies of 50 Hz (blue) and 22.9 Hz (red). The red line shows the clear periodic character of the forces produced by flapping.

While the raw measurement was noisy, the signal can be decomposed into several effects that correspond to the natural dynamics of the apparatus.

Fig. 3.10 shows a single-sided amplitude spectrum (normalized FFT) of the force measurement shown in Fig. 3.9. The three colors indicate the amplitude spectra of the raw measurement and the two filtered measurements. Note that the spectra of the two filtered measurements are equal to the spectrum of raw measurement below their respective cutoff frequencies, and drop to zero above their cutoff frequencies.

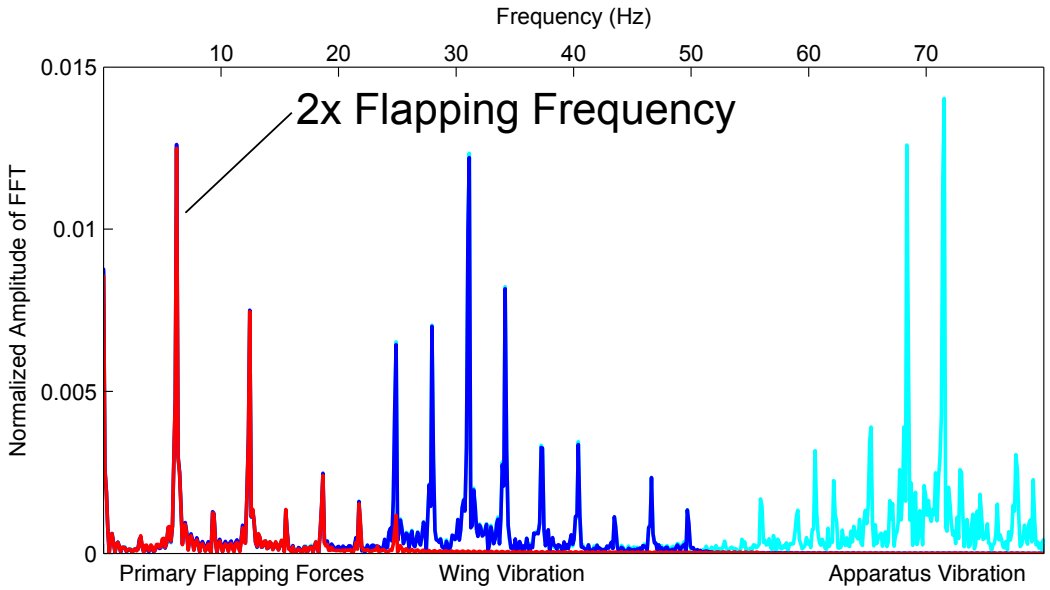

Figure 3.10: Amplitude spectrum of the force measured during flapping at ≈3 Hz, with the frequency bands of three major effects identified by color: Primary aerodynamic and inertial forces resulting from the flapping motion (red), vibration of the wing structure (blue) and high-frequency vibration of the force sensor apparatus (cyan). Lowpass filtering the force signal with the appropriate cutoff frequency preserves the primary forces while eliminating vibration effects. The strongest component of the primary force occurs at two times the flapping frequency, reflecting the symmetry between upstroke and downstroke in each cycle.

The phenomena of interest in these experiments were the aerodynamic forces resulting from flapping, which were assumed to occur at frequencies no

higher than several times the flapping frequency. To obtain a clean force profile for analysis, it was necessary to lowpass filter the signal at a frequency that would eliminate the effects of vibration while preserving the primary aerodynamic and inertial effects. This objective was accomplished by lowpass filtering each force measurement with a cutoff frequency of 7.5 times the flapping frequency, which was the approximate position of the trough in the amplitude spectrum between primary forces and wing vibration effects. This choice of cutoff frequency preserved maximum bandwidth of the sensor is comparable to the bandwidth achieved in other studies of flapping wings in air [45].

3.6 Motion Tracking

The kinematics of the flapping wings were tracked using the video frames recorded by the camera in the apparatus. The camera was a Casio EXILIM EX-FH20 model, recording color images at a rate of 210 frames per second at a resolution of 480x360 pixels. The lamps mounted to the experimental apparatus served to illuminate the wing and allowed the red color of the main wing beam to be detected in each video frame. Fig. 3.11 shows the top-down view of the high-speed camera used to measure flapping kinematics. The view area of the high-speed camera included both a top-down view of the flapping wing as well as a side view in the reflection of the mirror. During processing, these two regions were treated separately to obtain different kinematic variables. The motion tracking software was custom written for this application using MATLAB and various components of MATLAB's Image Processing Toolbox.

Kinematic data from these experiments were recorded using the coordinate

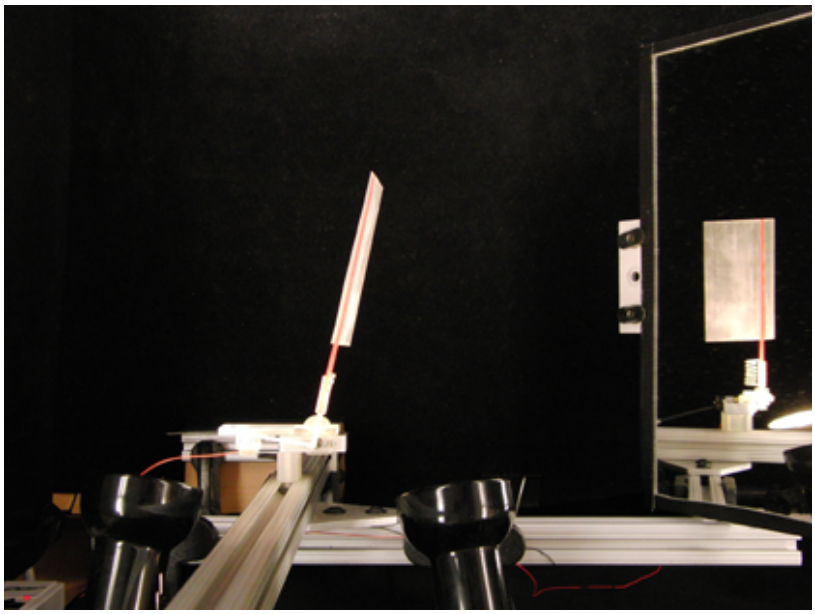

Figure 3.11: View area of experimental apparatus from the high-speed camera showing both top-down view of the wing and side view through the mirror.

system shown in Fig. 3.12, which was adapted from previous work on flapping wings in air [45]. The angles required to describe the position of the wing in the labratory frame are the stroke angle (ϕ), the deflection angle (ψ) and the out-of-plane deviation angle (θ). The figure shows the position of the mirror so that measurements made in the side view could be related to position of the wing in the top-down view. The stroke angle was measured with respect to the nominal position of the wing at mid-stroke, and the arrows in the diagram indicate positive angles.

3.6.1 Stroke Angle

Measurement of the stroke angle was based on color identification in each video frame. The main beam and top of the hinge of each wing were colored red using

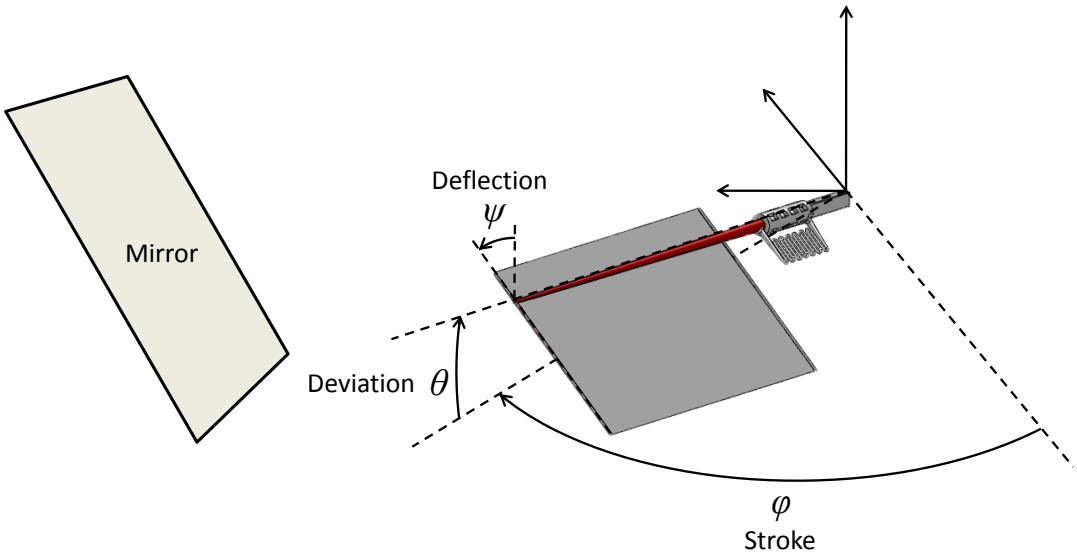

Figure 3.12: The coordinate system used in measuring the position of the wing in the laboratory reference frame, including the position of the mirror used for viewing the wing motion from the side. Arrows in the diagram indicate the direction of positive sign for each angle. The stroke angle was measured with respect to the mid-stroke wing position, so the motion was centered about a stroke angle of zero.

a permanent marker and the red color was brightly illuminated by the lamps mounted to the experimental setup. Fig. 3.13(a) shows a single video frame in the top-down view, in which the red portions are in line with the main beam. The pixels in this image were ranked according to their "redness." Isolating the red portions of the image presented a challenge due to the dim color perception of the high-speed camera, the uneven lighting and glare that occurred while flapping the wing, and the tendency of the image to become saturated if too much light was applied. Ultimately, a pair of 25-watt halogen lamps arranged as backlights provided relatively uniform lighting throughout the stroke of the wing without causing glare or saturating the camera. To quantify redness of each pixel in a RGB video frame, the green channel was simply subtracted from

the red channel and the resulting values were used to identify the points that were most likely to be on the main beam of the wing. Rather than other possible measures of redness, such as dividing the red channel by the overall intensity of the pixel, this scheme eliminated points in which the red and green channels were both saturated in a situation of intense glare from reflection off the wing surface.

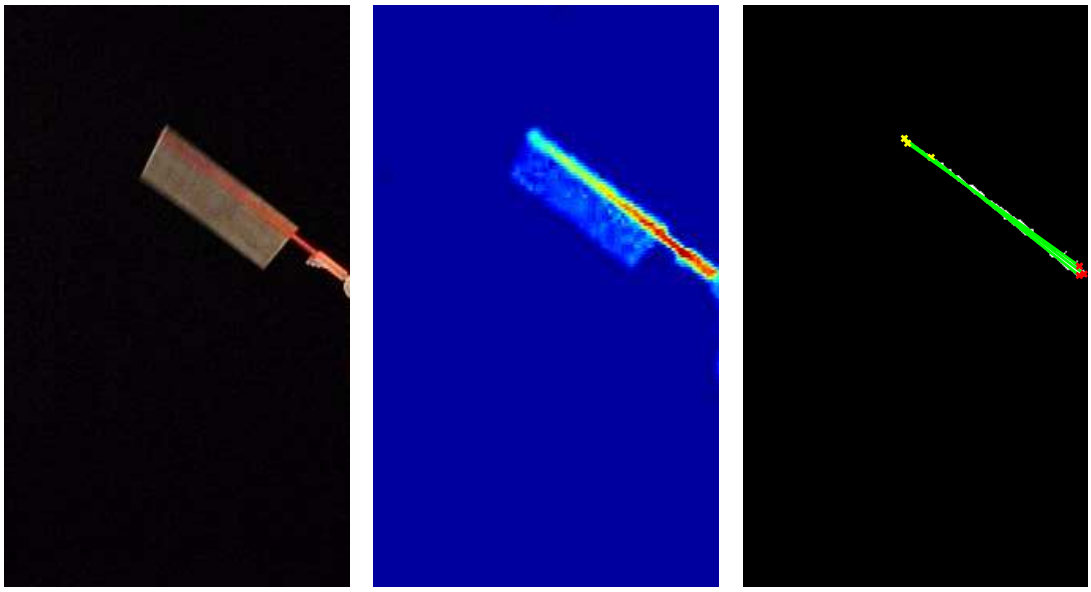

(a) (b) (c)

Figure 3.13: Original top-down view from high-speed video frame (a). Heat map of redness score for all points in the original video frame (b). High scoring (red) points were considered to belong to the main beam of the wing and were used for estimating the stroke angle. Red points overlaid with five lines produced by a Hough transform (c). The mean angle of these five lines was taken to be the stroke angle of the wing.

Fig. 3.13(b) shows a heat map representing the redness score of each pixel in the video frame. These redness scores were then sorted and the top 1000 points were considered to belong to the main beam. The Hough transform feature extraction technique was applied to these points to estimate the stroke angle using the MATLAB function `hough.m`, and the top five peaks in Hough-space were

converted into straight lines representing the main beam using `houghpeaks.m` and `houghlines.m`. The stroke angle was taken to be the mean angle of the five lines generated by the Hough transform. Fig. 3.13(c) shows the points with the highest redness scores, overlaid with the five lines generated by the Hough transform. the stroke angles measured using this method are shown in blue in Fig. 3.14. The mean value of these angles is shown in red, and was used as the measure of stroke angle in subsequent calculations.

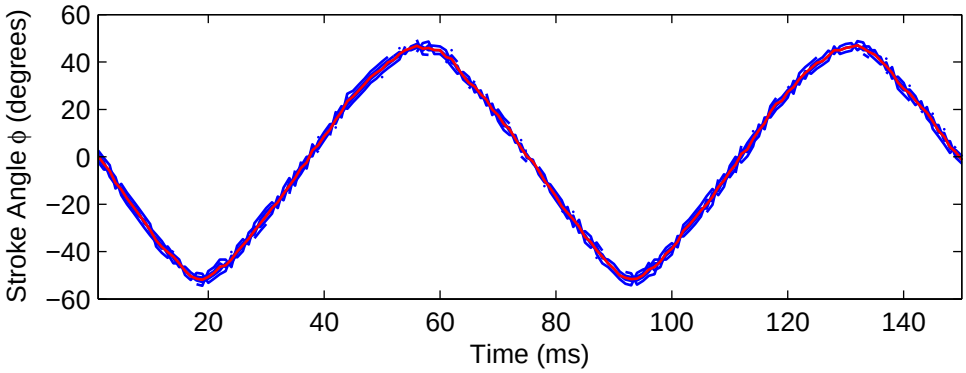

Figure 3.14: Measurement of stroke angle ϕ during two periods of flapping, showing angles of individual straight lines generated by the Hough transform (blue) and the mean value of these angles (red). The mean value was used as the stroke angle in subsequent calculations and analysis.

3.6.2 Deflection Angle

While flapping, the wings passively deflected to an angle of roughly ±45° and reversed their deflection angle with every reversal of direction in the wing's motion. This deflection angle was measured in two ways. The primary method of measurement was to calculate the area of the wing in the top-down view projected onto the plane of flapping and to compare the measured area to the

true area of the wing. Fig. 3.15(a) shows the top-down view converted to a binary image representing the area of the wing projected onto the stroke plane, and the area of the white region of this image was computed using the MATLAB function `bwarea.m`. Calibration of the area measurement was performed using video frames showing wings of known geometry mounted in fixed positions on the apparatus. Conversion factors were calculated to relate distances in millimeters to pixel distances measured in the video. Measurements were also performed to subtract off the area of the main beam, hinge, root and apparatus that appeared in the video frame but were not part of the area of the wing surface.

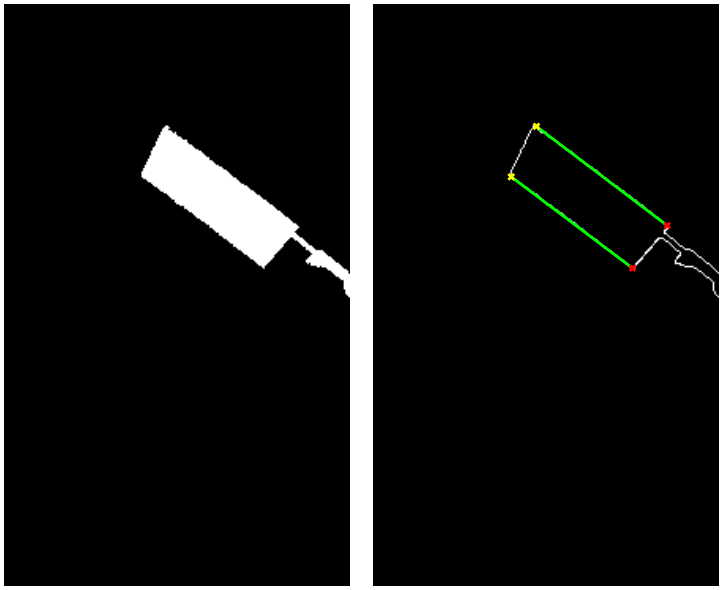

(a) (b)

Figure 3.15: Conversion of the top-down view to a binary image for computing the area of the wing projected onto the stroke plane (a). Edges of the projected wing area shown with leading and trailing edges identified using a Hough transform (b).

Using the measurement of projected area, the deflection angle was computed as $\pm \arcsin(\text{projected area}/\text{true area})$. The sign of the deflection angle was

determined by locating the center of area of the wing's projected area using the `centroid` option of the function `regionprops.m` and comparing its position to the location of the main beam previously found. When the wing's center of area was found to be to the left of the main beam in the top-down view, then the sign of the deflection angle was set to be positive and vice versa, in accordance with the angle convention previously defined.

The second measure of deflection angle was computed purely as a check on the first method, and relied on computing a Hough transform for the edges of the wing's projected area. Similar to the way the Hough transform was used to extract the stroke angle, it was also used to locate the leading and trailing edges of the wing in its deflected configuration, shown in Fig. 3.15(b). Then the perpendicular distance between these two lines was computed both at the wing root and wing tip and the mean of these distances was used as the chord length projected onto the stroke plane. A second measure of deflection was calculated as $\pm \arcsin(\text{projected chord}/\text{true chord})$, similar to the method using projected wing area. This method produced largely the same result as the projected wing area method, though the Hough transform did not perform reliably for small deflection angles and during wing flips as the outline of the wing became less clear. Fig. 3.16 shows the measured deflection angle over two periods of flapping. In this plot, the red line shows the deflection angle measured using the method of projected wing area and the dashed blue line shows the deflection angle measured from the projected distance between leading and trailing edges using the Hough transform. While the latter method was not as robust, it agreed closely with the projected area method when the wing was deflected to an angle greater than $\pm 35°$. The projected area method was used as the sole measure of deflection angle in subsequent calculations.

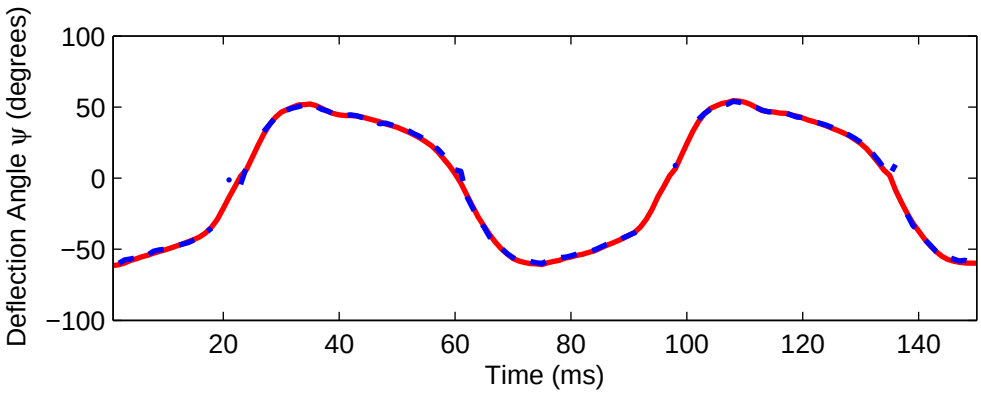

Figure 3.16: Measurement of deflection angle ψ during two periods of flapping, based on a method of projected wing area (red) and projected distance between leading and trailing edges (blue dashed). The method of projected wing area was used for deflection angle data while the method based on distance between leading and trailing edge was used for validation.

In order to include the mirror in the camera's field of view, it was necessary to position the camera away from vertical alignment with the axis of wing rotation in the stroke angle by a distance of 41 mm. Thus, with a wing positioned at stroke and deflection angles of zero, the line of sight in the top-down view intersected the main beam of the wing at an angle of approximately 4°, resulting in a bias in the measurement of the deflection angle. This bias angle varied with the stroke angle, from approximately zero when the wing was located directly beneath the camera at positive stroke angles, to approximately 6° at negative stroke angles. To account for this bias, a wing was fixed at a deflection angle of zero and flapped slowly while recording the kinematics from high speed video. The apparent deflection angle was calculated using the same process used in all experiments and a fourth-order polynomial was fit to the data. This polynomial represents the nominal apparent deflection angle as a function of stroke angle, and was subtracted from the measured deflection angle. Fig. 3.17 shows

the stroke angle and measured deflection along with the calculated correction and the corrected deflection angle. This correction was applied to the measured deflection angle in all experiments.

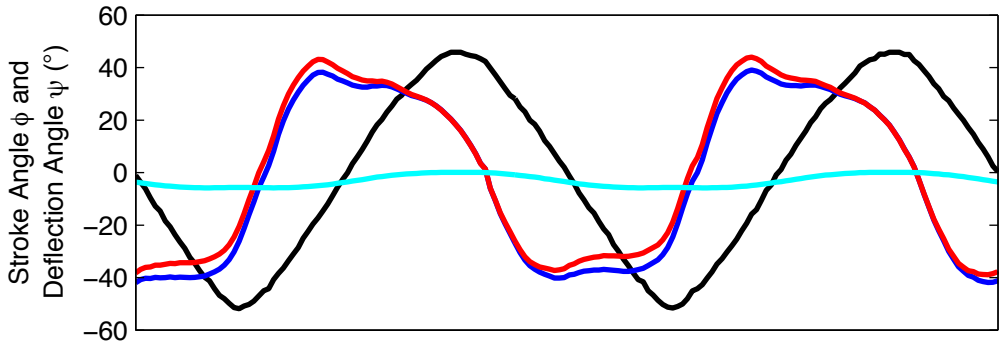

Figure 3.17: Measured deflection angle ψ during two periods of flapping (blue) with calculated correction for the nominal apparent deflection angle (cyan). Stroke angle (black) is shown for reference. Corrected deflection angle (red) aligns with the measured deflection at positive stroke angles and deviates from it at negative stroke angles. The corrected deflection angle was used in all subsequent calculations.

3.6.3 Deviation Angle

While the wings and flapping apparatus were designed to prohibit motion of the wing out of its horizontal stroke plane, some out-of-plane motion did occur in practice due to flexibility of the wing structure and tolerances in the assembly. These small amplitude motions in the vertical direction contributed to the measured lift force through inertial effects of bouncing or aerodynamic effects caused by the change in the wing's instantaneous angle of attack. As the wing underwent motions out of the horizontal stroke plane, the wingtip moved up and down in the side-view provided the mirror, allowing a relatively straight-

forward calculation to extract the deviation angle by tracking the vertical motion of leading and trailing edges at the wingtip. To locate the corners of the wingtip, the side-view of the wing was converted to a binary image to find the outline of the wing. Then the points on the outline were segmented into quadrants with respect to the center of area of the wing such that the leading and trailing edge corners were in separate quadrants. Then the points in each quadrant were ranked according to a distance metric that separately weighted horizontal and vertical distance from the center of area:

$$position\ score = \frac{10}{dist_y} + \frac{1}{dist_x} \tag{3.1}$$

The distance from the center of area in the y-direction was weighted more heavily to ensure that the highest scoring points were located on the leading or trailing edges. The top 10 points in each quadrant were considered to be the points on the leading or trailing edges that were farthest from the center of area, and therefore gave an accurate estimate of the vertical position of the wing corners. Fig. 3.18(a) and Fig. 3.18(b) show the center of area of the side-view of the wing and the points used to track the vertical motion of the leading and trailing edges at the wingtip. The effective wingtip was considered to be located at the tip of the main beam. This position was calculated as a point between the leading and trailing edge corners, using the known wing geometry.

In contrast with the top-down view of the video frame, the side-view required significant correction for geometric and optical effects of the setup. The first correction was to subtract off any nominal perceived vertical motion of the wingtip that resulted from the view angle of the mirror, and the second correction was to adjust the scale of perceived motion to account for perspective as the wing flapped toward and away from the mirror.

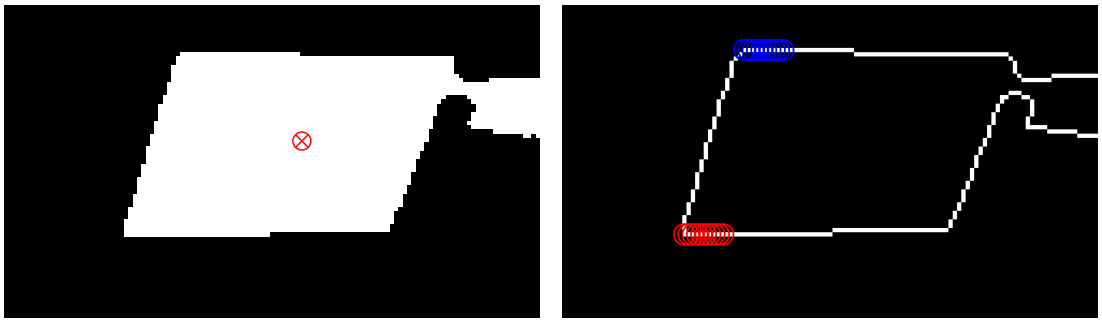

(a) (b)

Figure 3.18: Binary image of side-view with center of area shown in red (a). Edge of the binary image showing points chosen for measuring the vertical positions of the leading and trailing edges at the wingtip (b).

In the first correction, the mirror providing the side-view of the wing was positioned to provide a line of sight parallel to the horizontal plane of flapping and to keep the wing within the field of view at every point of the wing stroke. However, to correct for misalignment, the nominal motion of the wingtip was recorded and subtracted off from measurements made during actual flapping experiments. The nominal motion of the wingtip was captured by recording the wing moving slowly back and forth with zero deflection. During this slow flapping motion, the corners of the wingtip were tracked and the position of the tip of the main beam was calculated using the same method as described for the process of recording deviation angle. A cubic polynomial was fit to describe the vertical height of the wingtip as a function of the stroke angle, and this nominal motion was subtracted off all subsequent measurements. Fig. 3.19 shows the recorded vertical motion of the wingtip during a slow flapping motion with the polynomial function used to describe it and the resulting vertical position of the wingtip once the polynomial calculation was subtracted. Note that the nominal vertical position of the wing in the camera frame is arbitrary.

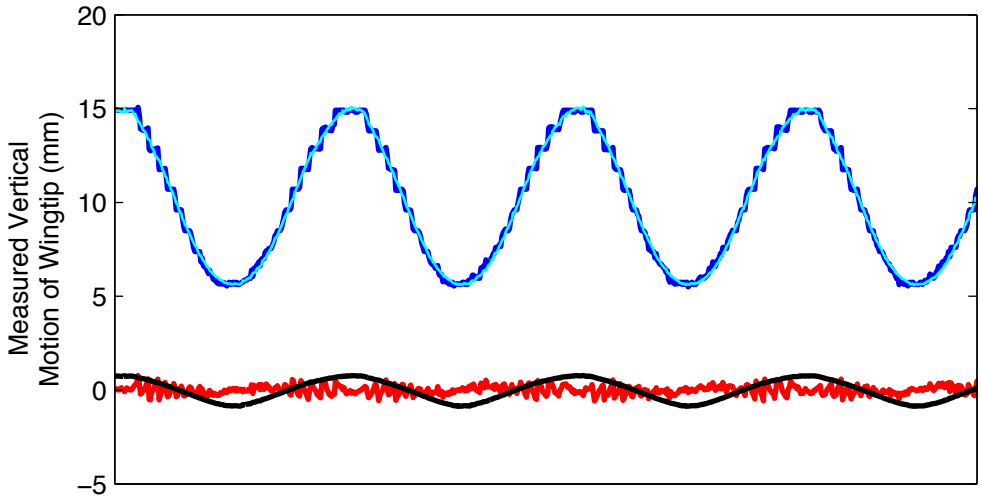

Figure 3.19: Recorded vertical motion of the wingtip (blue) during slow flapping with polynomial calculation used to describe this nominal motion (cyan). When the polynomial calculation was subtracted from the nominal motion, the resulting measurement was flat and centered about zero (red). The stroke angle (black) is shown for reference and is plotted in radians.

The positions of the wingtip corners were also used to make the second correction. Here, the distance between these corners (i.e. the known chord length of the wing) was measured at every stroke angle and a cubic polynomial was fit to describe the relationship between perceived scale factor and the wing position. Using this cubic polynomial, a correction was applied to the apparent motion seen in the side-view. This correction had the effect of slightly increasing the amplitudes of out-of-plane motions when the wing was far from the mirror (which appeared smaller), and slightly decreasing the amplitudes of out-of-plane motions when the wing was near the mirror (which appeared larger). Fig. 3.20 shows the corrected deviation angle, indicating very small deviations from the horizontal stroke plane, but with a periodic pattern of motion nevertheless.

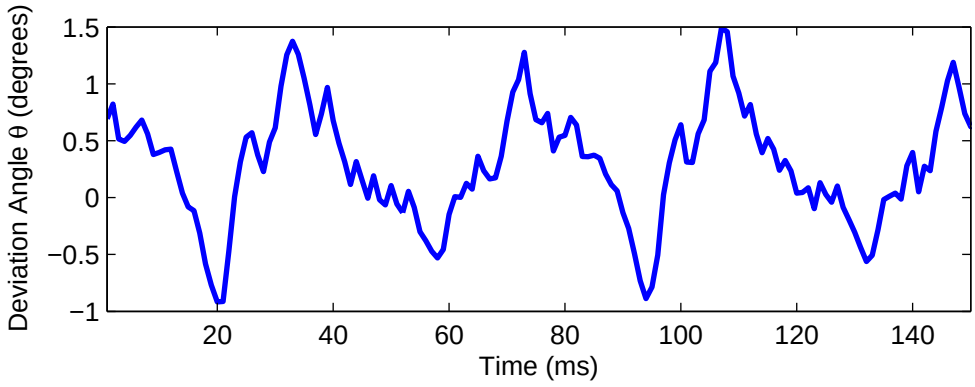

Figure 3.20: Measured deviation angle θ during two periods of flapping.

3.6.4 Data Alignment, Smoothing and Registration

Precise temporal alignment of the video and force measurement was crucial for accurate calculations. To accomplish the alignment, five impulses were delivered to the wing driving mechanism using a swinging mass, both at the beginning and at the end of each test run. Then, the moments of impact between the mass and the apparatus were manually identified in the video and in the recorded force data. Fig. 3.21 shows the frame of impact between the swinging mass and the apparatus. Five successive impulses were used to ensure accuracy and to prevent errors resulting from the lower sampling frequency of the camera compared to the sampling frequency of the force sensor. The frame locations of the five impulses at the beginning and end of each experiment were averaged, and the average values were used to pin together the start and end of the video and measured force data. Finally, the kinematic data extracted from the video was resampled from its original 210 Hz to the 1 kHz sampling rate of the force sensor using `resample.m`.

Smoothing of the stroke, deflection and deviation measurements was accom-

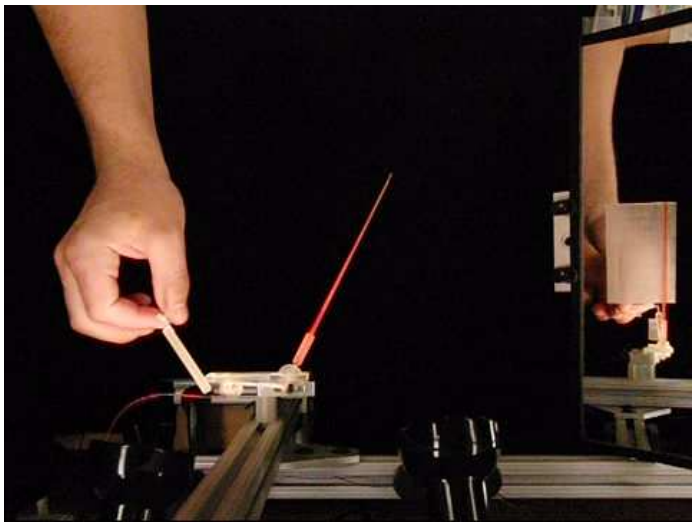

Figure 3.21: Video frame showing impact between a swinging mass and the wing driving mechanism mounted on the load cell. Delivering an impulse to the load cell apparatus produced an identifiable moment of impact in both the video and the force measurement, allowing precise synchronization of these two sets of data. Five impulses were delivered manually to the apparatus at the beginning and end of each data collection run. The moments of impact were recorded manually from the video and the measured force.

plished with a sliding polynomial technique with third order polynomials and a window size of 51. This method entailed fitting a polynomial to the window of data surrounding a point and then evaluating the polynomial at that point and repeating for each data point in the experiment. This method also enabled analytical differentiation of the polynomials to provide first and second derivatives of each kinematic variable without the noise accumulated by a crude difference method of numerical differentiation.

During each experiment, wings were flapped at five different speeds, controlled manually by modulating the voltage from the DC power supply. At each

of these speeds, the wings were allowed to flap for 10-20 cycles. During analysis, these windows of constant-speed flapping were manually identified so that they could be registered and averaged together. Synchronizing samples for registration was accomplished by identifying the peaks in the stroke angle using `findpeaks.m` and overlaying the data from each wing stroke, aligning them temporally using the peaks in the stroke angle. Figures 3.22 through 3.25 show a representative set of data collected from a wing flapping at a constant speed for 18 cycles. The measured force and kinematic variables showed great regularity, indicating that the average of these 18 cycles was a suitable representative sample for subsequent calculations.

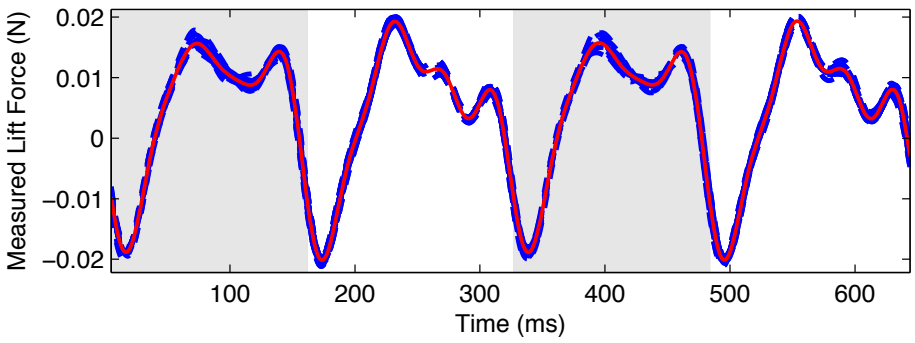

Figure 3.22: Registered force from 18 strokes (blue), with mean used in subsequent calculations (red).

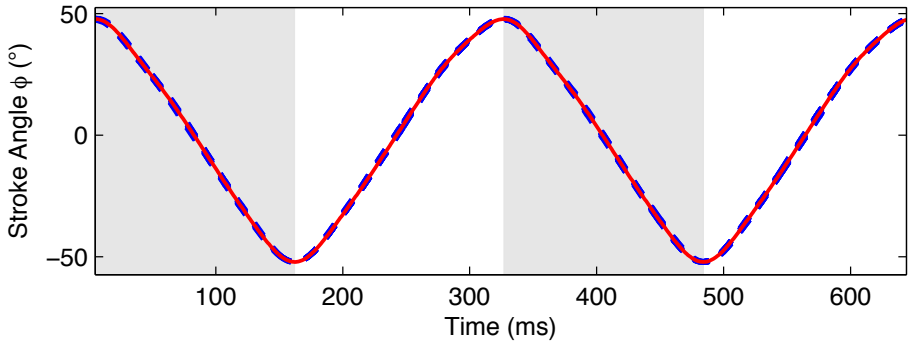

Figure 3.23: Registered stroke angles from 18 strokes (blue), with mean used in subsequent calculations (red).

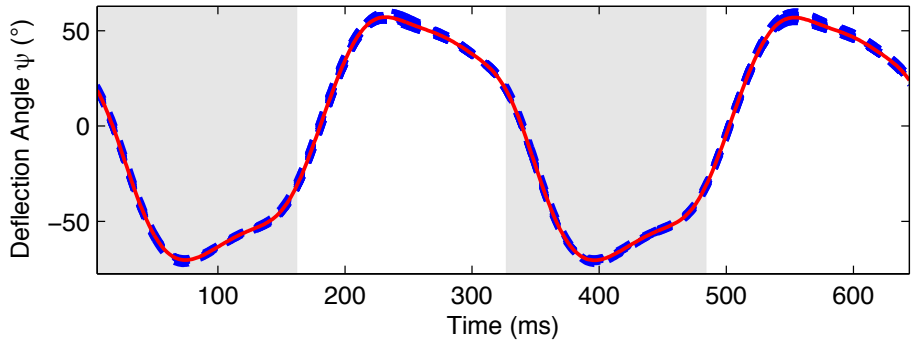

Figure 3.24: Registered deflection angles from 18 strokes (blue), with mean used in subsequent calculations (red).

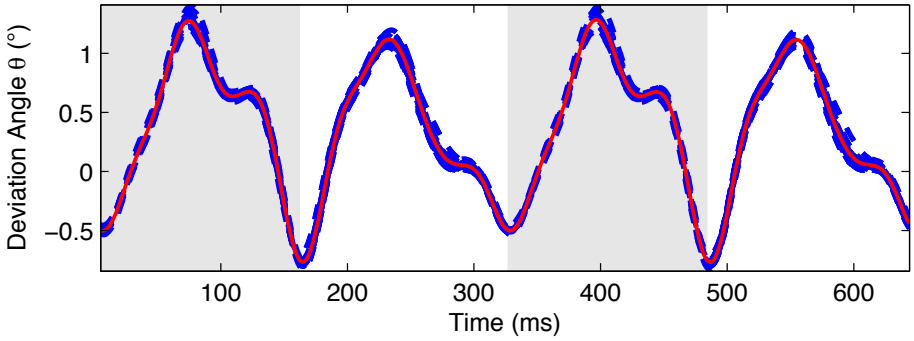

Figure 3.25: Registered deviation angles from 18 strokes (blue), with mean used in subsequent calculations (red).

3.6.5 Range of Parameters Explored

Experiments were conducted on eleven different rectangular wings varying in chord length and span. Wings featured seven different chord lengths between 40 mm and 80 mm and five different wing spans varying between 40 mm and 120 mm. Fig. 3.26 shows all eleven wings tested. Flapping amplitudes were varied between three possible settings of 72°, 81°, and 96° and flapping speeds were varied from approximately 1 Hz to 4 Hz, resulting in a range of Reynolds numbers (Re) between 2500 and 5000. These values represent the size scale and range of Reynolds numbers of large insects and ornithopters.

In total, 68 sets of data were recorded, each representing a distinct combination of wing geometry, flapping speed and amplitude. Independently varying these parameters was important for identifying the effects and contributions of each one, and helped to prevent over-fitting in data-driven models. In the process of modeling lift forces through symbolic regression, it was critical to provide data from many different experiments simultaneously, thereby ensuring that the resulting equations reflect the physical phenomena underlying all experiments as well as capture the effects of variation in wing geometry and flapping kinematics.

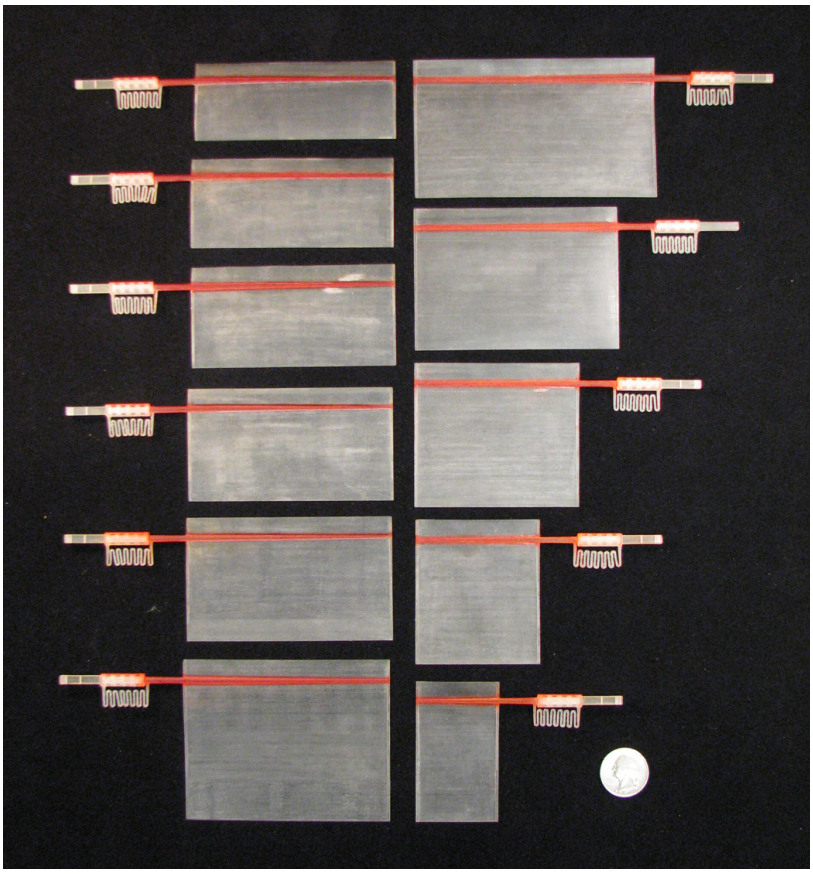

Figure 3.26: All eleven wings used in flapping lift force measurements. The wings are arranged to show variation in chord length (40-80 mm) and span (40-120 mm).

CHAPTER 4

ANALYSIS AND RESULTS

4.1 Introduction and Review of Existing Work

Many studies have developed equations and solution techniques to estimate the forces associated with the flapping motion of insect wings. Some have focused on the inertial forces [16], while aerodynamic studies have generally focused on either numerical solutions of Navier-Stokes equations in two or three dimensions [48, 42], or on quasi-steady approximations of the observed behavior [33, 14]. The Navier-Stokes equations offer important insights into the full character of the fluid around the wing including vorticity and fluid-structure interaction, but are difficult to calculate and computationally expensive. Quasi-steady approximations, in contrast, capture most of the character of the aerodynamic forces without any detailed modeling of the fluid flow, and have been applied to predict the forces on a flat surface such as a wing or tumbling plate. Numerical methods and quasi-steady approximations have both been compared to experimental data obtained from an apparatus measuring the forces on a flat plate reproducing insect-like flapping kinematics in liquid [44].

In this chapter, several quasi-steady equations from literature are compared against force measurements obtained from flapping wings in air. Then, a data-mining approach is applied to develop new equations describing the data to examine whether this process can improve upon existing equations or shed new insight into the aerodynamic phenomena. The data-mining process used here was based on the Eureqa symbolic regression software [34]. Symbolic regression is a method of searching for equations based on evolutionary computation

[23, 19] that has already been used to model complex systems defined by explicit [13, 17, 4], implicit [36], iterated [35] and differential equations [7]. The performance of all analytical and data-driven models is illustrated by plotting their lift predictions against measured data from ten randomly selected experiments that were reserved as testing data and were not used in Eureqa to train data-driven models.

4.2 Inertial Force Calculations

The total vertical force measured during flapping experiments is a combination inertial and aerodynamic forces, which contributed roughly equally to the overall shape of the force profile produced by a flapping wing. In order to compare analytical estimates of aerodynamic forces with experimental measurements, it is necessary to account for the associated inertial forces. In the evaluation of each analytical model presented here, inertial forces were calculated and added to the lift estimate, producing a complete force profile that could be compared to the measured vertical force.

Wings flapping on the experimental apparatus underwent rapid changes in their deflection angle (often termed 'wing flips') near the moments of stroke reversal. These rapid wing flips, and any other changes in the wing's deflection angle over the course of a wing stroke, have associated inertial forces that were measured by the load cell. Due to the mass of 3D printed wings compared to their surface area, these inertial forces accounted for approximately half of the measured forces in most experiments. To model the effects of these inertial effects, the flapping wing was considered to act as a compound pendulum com-

posed of the volume of the thin wing surface pivoting about the axis of rotation as shown in Fig. 4.1.

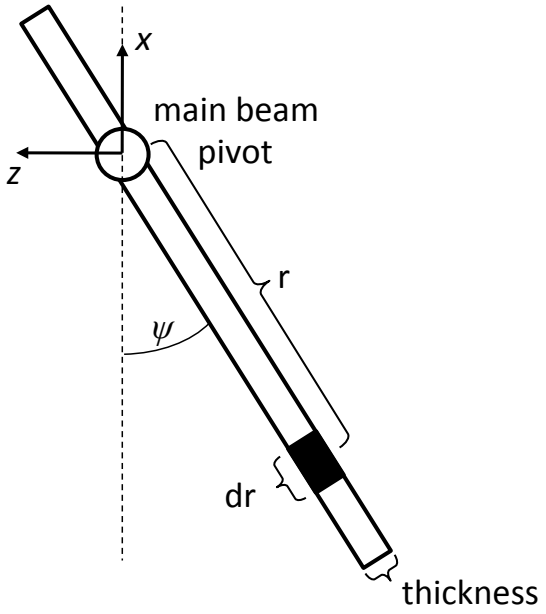

Figure 4.1: Diagram of wing as a compound pendulum for calculating inertial forces, viewed along the axis of the main beam.

Deriving the equations of motion for this compound pendulum begins by twice differentiating the vertical location of the element *dr*:

$$x_{dr} = -r\cos\psi \tag{4.1}$$

$$\dot{x}_{dr} = r(\dot{\psi}\sin\psi) \tag{4.2}$$

$$\ddot{x}_{dr} = r(\ddot{\psi}\sin\psi + \dot{\psi}^2\cos\psi) \tag{4.3}$$

The element *dm* is a span-wise strip of mass and is defined as:

$$dm = dr \cdot thickness \cdot span \cdot \rho_{material} \tag{4.4}$$

Equating $dF_x = \ddot{x}_{dr}dm$ and integrating yields:

$$F_{x,pendulum} = \frac{1}{2} \cdot thickness \cdot span \cdot \rho_{material} \cdot (\ddot{\psi}\sin\psi + \dot{\psi}^2\cos\psi) \cdot (c_{leading}^2 - c_{trailing}^2) \tag{4.5}$$

where $c_{leading}$ and $c_{trailing}$ indicate the distance from the pivot point (main beam) to the leading edge and trailing edge of the wing, respectively. While this pendulum motion was the primary inertial effect measured by the force sensor, there was also a secondary effect caused by the small bouncing motions of the wing out of the flapping plane. These bouncing motions accounted for some of the small ripples observed in the lift profile but did not contribute significantly to the overall structure of the force profile. Applying a similar calculation using chord-wise mass elements results in a similar expression for the inertial force caused by out-of-plane deviation:

$$F_{x,deviation} = \frac{1}{2} \cdot thickness \cdot chord \cdot \rho_{material} \cdot (\ddot{\theta} \cos\theta + \dot{\theta}^2 \sin\theta) \cdot (span_{root}^2 - span_{tip}^2) \quad (4.6)$$

where $span_{root}$ and $span_{tip}$ indicate the span-wise coordinates of the most proximal and distal points on the wing surface, measured from the origin at the root of the wing. These dimensions are shown in Fig. 4.2 along with the chord-wise mass element. The total calculated inertial reaction force $F_{inertial}$ is equal to the sum $F_{x,pendulum} + F_{x,deviation}$.

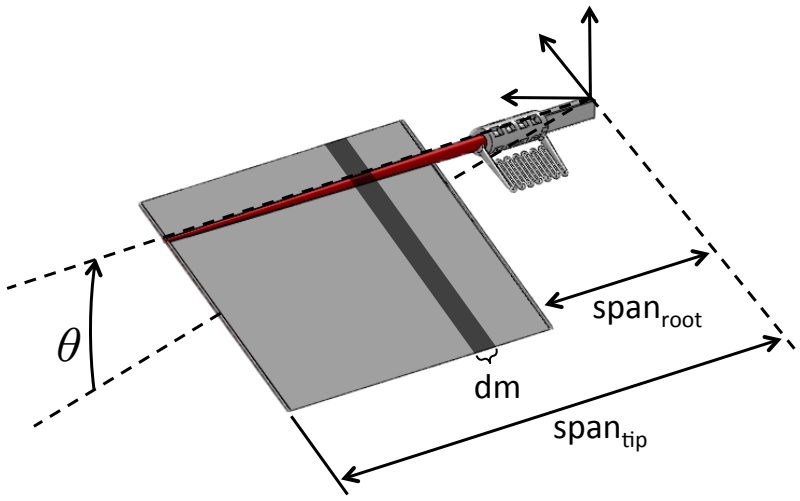

Figure 4.2: Diagram of the chord-wise mass element used to calculate the inertial forces caused by out-of-plane deviation.

Fig. 4.3 shows the contributions of inertial force from the pendulum motion and the out-of-plane deviation compared to the total measured force in one experiment. The overall shape of the inertial force calculation qualitatively matches the shape of the total measured force, including the approximate shapes of the three small ripples observed during each stroke of the wing, along with the large negative peak separating each downstroke and upstroke. As seen in this plot, the inertial force largely accounts for the negative peak that occurs during the rapid wing flip and the positive peak immediately following it, which occurs as the wing overshoots its new deflected position and rebounds off the force of the spring opposing its rotational motion. As a check, the mean value of the calculated inertial force is approximately zero, which is consistent with the fact that inertial forces cannot cause a mean lift force. The difference between the measured force and the calculated inertial reaction is considered to be due to aerodynamic lift.

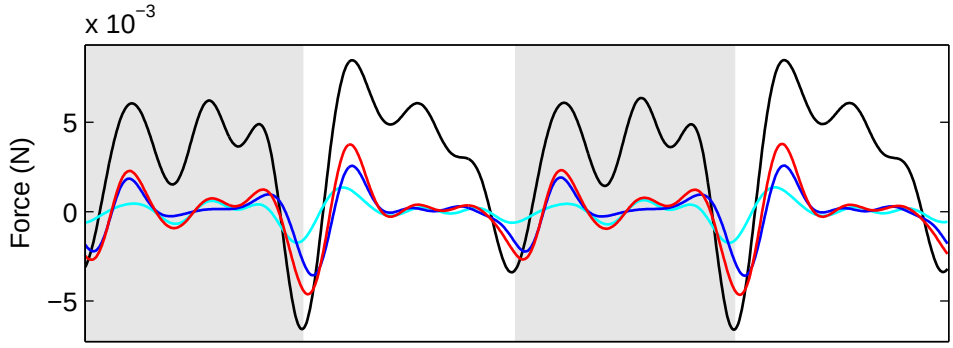

Figure 4.3: Calculated inertial force for one experiment (red) as the sum of forces due to pendulum motion (blue) and out-of-plane deviation (cyan), shown with the total measured force (black). The pendulum motion provides the primary contribution of inertial forces.

4.3 Analytical Models

For the purposes of designing and controlling an ornithopter, it is useful to have a set of equations for predicting the forces produced by a flapping wing that are simple yet accurate. One of the main purposes for performing experiments on flapping wings was to evaluate existing models and to propose new ones, so several different quasi-steady models were chosen from the literature and compared against experimental results. These models included a standard planar estimate proportional to velocity-squared and two more sophisticated models that have been applied to flapping wings [45] as well as fluttering and tumbling plates [2, 3, 26].

4.3.1 Translational Lift Proportional to Velocity Squared

The first analytical model explored was the estimate of lift proportional to the square of the translational velocity of the wing L_{trans}:

$$L_{trans} = \frac{1}{2}\rho v^2 A C_L \tag{4.7}$$

where v is the wing velocity, ρ is the fluid density, A is the area of the wing surface, and C_L is the coefficient of lift. The theoretical value of the coefficient of lift depends on the angle of attack α:

$$C_L = C_{Lmax} \sin 2\alpha \tag{4.8}$$

This model was evaluated by adding it to the estimate of the inertial forces (with and without including the inertial forces of out-of-plane deviation) and fitting the coefficient C_{Lmax} with the nonlinear regression function `nlinfit.m`

in MATLAB. In this case, this equation is considered a planar model and termed L_{planar} because it was evaluated using only the wing's motion in the nominal stroke plane ($\dot{\phi}$), though in subsequent calculations it was adapted to include the wing's out-of-plane velocity ($\dot{\theta}$). When the wing's out-of-plane velocity is included, the model is termed L_{trans}. Fig. 4.4 shows this model evaluated on four sets of experimental data taken from the set of ten experiments reserved for model testing. The model including the inertial effects of out-of-plane deviation shows better qualitative agreement with the measured forces as it captures more of the subtle ripples in the force profile. The values of C_{Lmax} fit through nonlinear regression ranged from 1.61 to 2.23, with a mean C_{Lmax} of 1.92 ignoring inertial forces from out-of-plane deviation, and a mean of 1.87 when those inertial forces were included. These values are close to the standard value of 1.8 for *Drosophila*.

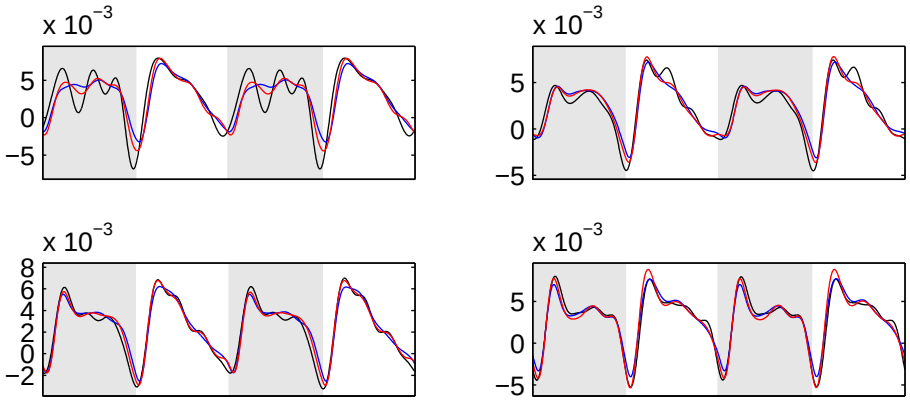

Figure 4.4: Force predictions of planar velocity-squared lift added to the inertial forces of the pendulum motion only (blue) and the total inertial force calculation including out-of-plane deviation (red), plotted with the measured force (black) for comparison on four randomly selected sets of experimental data. Given its simplicity, this model shows strong overall agreement with the measured force.

4.3.2 Lift Equations of Whitney and Wood

The second analytical model considered was used in another study of flapping wing lift production by a robotic wing in air [45], and is a sum of two components: Translational lift and added mass effects. The first component is simply L_{trans}, calculated using the wing's total translational velocity including both stroke velocity ($\dot{\phi}$) and velocity of out-of-plane deviation ($\dot{\theta}$). This calculation utilizes an angle of attack that is not simply the angle between the wing surface and the stroke plane, but rather the angle between the wing surface and its direction of incident flow (i.e. the total velocity vector of each blade element of the wing). The second component in this model is an added-mass calculation, which is a sum of two terms, one proportional to the wing's linear acceleration (primarily determined by $\ddot{\psi}$) and another proportional to its rotational acceleration ($\ddot{\psi}$) [37]. The added mass lift proportional to linear acceleration is termed AM_{trans} and is shared by other models examined in this study, while the added mass lift proportional to rotational acceleration, termed AM_{rot}, is unique to this model. Nominal coefficient values for these added mass terms were taken from the theoretical literature and are related to the geometry of the wing and density of the fluid, representing a volume of fluid surrounding the wing surface. However, for the purposes of computing model accuracy, additional coefficients ($\beta_{trans}, \beta_{rot}$) were appended to these added-mass terms and were fit using nonlinear regression along with the coefficient of lift in the model.

This model was evaluated with and without the added mass terms included. In the case where added mass terms were excluded, the model reduced to a simple velocity-squared equation that differed from the planar velocity-squared model only by including the out-of-plane velocity of the wing in calculation of

the total velocity and angle of attack. However, since the out-of-plane motion was confined to approximately ±1° above and below the stroke plane, these effects were minimal and the calculation was nearly indistinguishable from the planar lift calculation.

The added mass terms, however, make a significant improvement to the accuracy of calculation. Fig. 4.5 shows this model compared with the measured forces after fitting only C_{Lmax} and leaving β_{trans} and β_{rot} equal to 1. The calculation including added mass terms shows better qualitative agreement in regions near the prominent negative peaks associated with stroke reversal and wing flips where linear and rotational accelerations are the greatest. Fig. 4.6 shows the individual aerodynamic components of the Whitney-Wood equations compared with the total measured force, highlighting the contributions of the added mass terms near wing reversal.

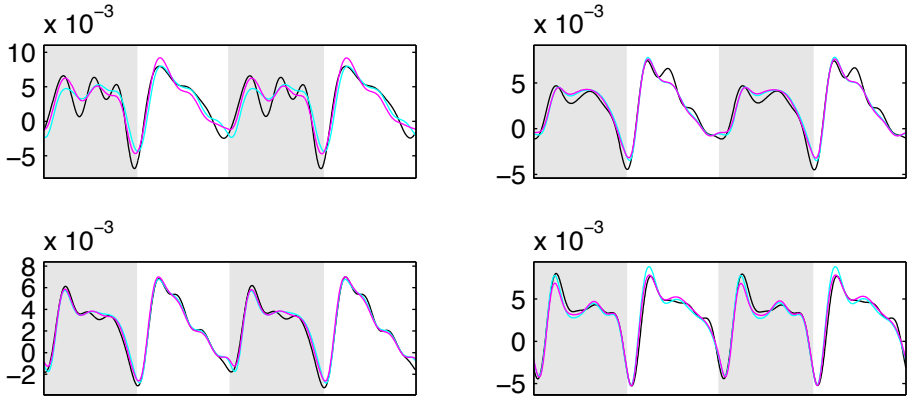

Figure 4.5: Force prediction using the equations of J. Whitney and R. Wood without the added mass terms (cyan) and with the added mass terms (magenta) on four sets of experimental data. In most experiments, the inclusion of the added mass terms resulted in an improved qualitative and quantitative fit to the measured force (black), especially around the wing flips where wing accelerations are greatest.

One of the important effects of the added mass terms is to shift the apparent temporal alignment of the force prediction compared to the force measurement. As observed in Fig. 4.5, the calculation omitting the added mass terms appears to lag behind the force measurement around the negative peaks in the force profile. However, when the added mass terms are added in, the alignment is improved. The underlying cause of this effect can be seen in Fig. 4.6, where the added mass lift caused by linear acceleration of the wing indicated by the green line becomes negative preceding the wing flip and then rapidly reverses to become positive as the wing flip proceeds. Adding this term to the pure inertial force prediction has the effect of shifting the location of the total calculated negative force peak earlier in time to align with the measured force peak.

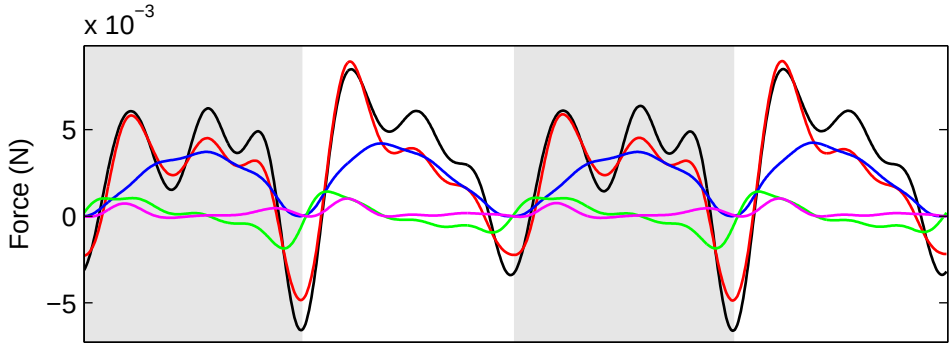

Figure 4.6: Calculation of the individual aerodynamic terms in the Whitney-Wood model, including velocity-squared lift (blue), added mass lift due to wing acceleration (green) and added mass lift due to rotational acceleration of the wing about the axis of deflection (magenta). Also shown is the total prediction (red) compared to the measured force (black).

Fitting all three coefficients (C_{Lmax}, β_{trans} and β_{rot}) gives the values shown in Table 4.1. The results of fitting coefficients reveal that C_{Lmax} has the most consistent value across all experiments. The mean value of β_{trans} across all 68 exper-

iments is close to zero and the mean value of β_{trans} is negative, indicating that these added mass effects do not exhibit their theoretical behavior. The inconsistency in coefficient values, observed in the standard deviation values, suggests that these added mass terms serve more as a fine tuning mechanism to improve the accuracy of the model rather than an indication of meaningful aerodynamic effects.

Coefficient	**Mean Value**	**Standard Deviation**
C_{Lmax}	1.88	0.25
β_{trans}	0.07	0.54
β_{rot}	-0.51	0.86

Table 4.1: Coefficients in the Whitney-Wood equations, fit using nonlinear regression on each of the 68 distinct data sets. The mean values and standard deviations are shown. The value of C_{Lmax} is the most consistent across all experiments, followed by β_{trans}. The negative value of β_{rot} and high standard deviation compared to the mean indicates that the effect of F_{rot} is small and inconsistent across experiments.

4.3.3 Lift Equations of Pesavento and Wang

The third analytical model considered was developed to characterize the fluttering and tumbling behavior of falling plates with Reynolds numbers around 1000. Like the previous model, these equations include a velocity-squared lift term and a pair of added-mass terms. However, these equations include slightly different added mass terms. Instead of AM_{rot}, this model includes an added mass term proportional to the product of the wing's rotational and translational velocity, termed $AM_{trans,rot}$. This model also includes an additional lift term proportional to these same variables, but with the opposite sign, and is termed L_{rot}. This rotational lift term includes its own coefficient of lift C_{Rmax} in addition to the coefficient of translational lift C_{Lmax}.

Fig. 4.7 shows the Pesavento-Wang model compared to the same four experiments. In this model, both added mass terms are proportional to the same element of the added-mass tensor, so this tensor value was augmented with a coefficient termed β_{AM}. Therefore, the added mass effects were not fitted separately, but instead were tuned together as a function of this single parameter.

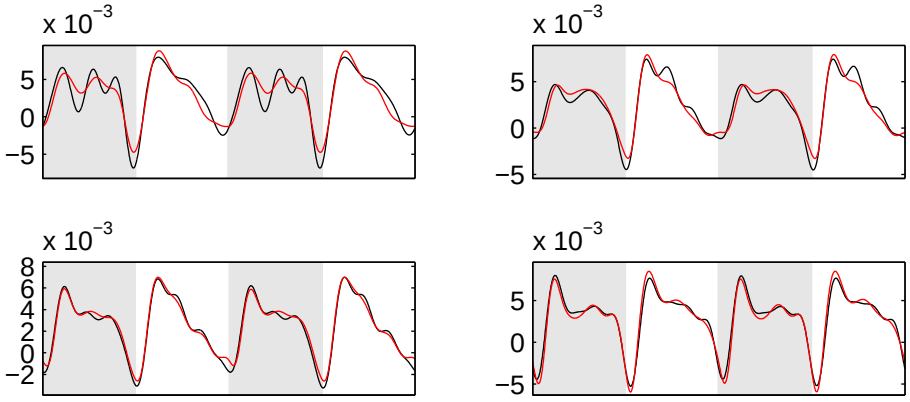

Figure 4.7: Force prediction using the equations of U. Pesavento and Z. J. Wang (red) compared to the measured force (black). Compared to other models, the Pesavento-Wang equations feature improved qualitative and quantitative agreement with the structure of sub-peaks in the force profile, as well as close alignment with the negative peaks associated with wing flips.

It is instructive to examine the contributions of individual terms in this equation to qualify the differences with the Whitney-Wood equations. These two models share two identical terms: 1) Translational velocity-squared lift and 2) added mass lift proportional to the linear acceleration of the wing. The Pesavento-Wang equations differ in their use of a second added mass term proportional to the product of translational speed and rotational speed as well as a second circulation-lift term, also proportional to the product of these two quantities. The Pesavento-Wang model does not include an added mass term pro-

portional to the wing's rotational acceleration, as was included in the Whitney-Wood model. Fig. 4.8 shows the individual contributions of all terms in the Pesavento-Wang equations.

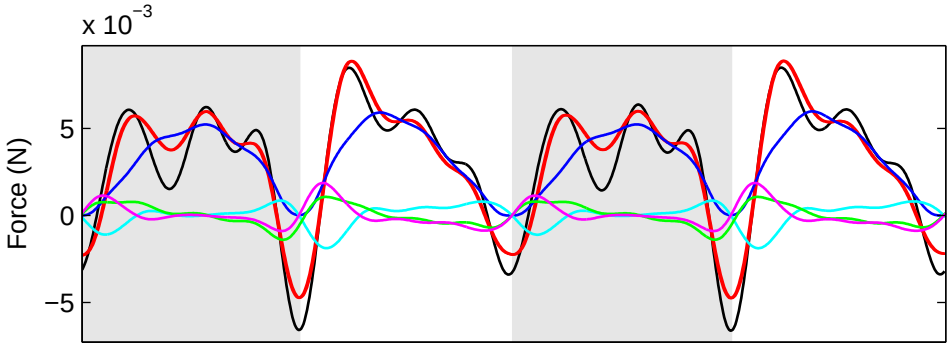

Figure 4.8: Calculation of the individual aerodynamic terms in the Pesavento-Wang model, including velocity-squared lift (blue), circulation-lift proportional to the product of translational speed and rotational speed (cyan), added mass lift due to wing acceleration (green) and added mass lift proportional to the product of translational speed and rotational speed (magenta). Also shown is the total prediction (red) compared to the measured force (black), showing strong qualitative agreement with the structure of individual peaks and precise alignment of the negative peaks associated with wing reversal.

The contribution of the second circulation-lift term (cyan) almost precisely negates the contribution of added mass lift proportional to linear acceleration after fitting C_{Rmax}. The effect of the second added-mass term, however, is greater than the corresponding term in the Whitney-Wood equations, and shows a prominent negative contribution at the start of the wing flip before quickly reversing to produce a positive peak, as observed in the linear-acceleration added mass term. Using C_{Lmax} and C_{Rmax}, it may be easier to tune this model to match an experimental measurement than the Whitney-Wood model. Indeed, fitted values of C_{Rmax} had a standard deviation much higher than the standard devi-

ation of C_{Lmax}, making it difficult to assess the applicability of this term to the flapping kinematics or the range of Reynolds numbers explored in these experiments. Table 4.2 gives the mean values and standard deviations of the lift and added mass coefficients.

Coefficient	Mean Value	Standard Deviation
C_{Lmax}	1.68	0.26
C_{Rmax}	1.25	0.70
β_{AM}	0.70	0.39

Table 4.2: Coefficients in the Pesavento-Wang equations, fit using nonlinear regression on each of the 68 distinct data sets. The mean values and standard deviations are shown. As in the Whitney-Wood equations, the value of C_{Lmax} is the most consistent across all experiments. The standard deviation of C_{Rmax} indicates inconsistency in this effect, which could be caused by the large variation in wing chord lengths used in experimentation. In contrast with the Whitney-Wood equations, the value of β_{AM} is close to 1 with a standard deviation less than the mean value, indicating that this model may give a more consistent prediction of added mass effects than the Whitney-Wood added mass terms.

4.4 Data Driven Models

For comparison with the analytical models, a data mining approach was also used to develop symbolic models describing the measured lift forces. The software used to produce symbolic models was Eureqa, a symbolic regression program based on evolutionary computation [34]. Fig. 4.9 shows a screenshot of the software performing a model search on the experimental data. The screen contains a list of candidate models, a plot comparing one of the listed models to the data, and an accuracy/complexity (Pareto) front showing all listed models.

The strategy for modeling lift forces with Eureqa was to train candidate

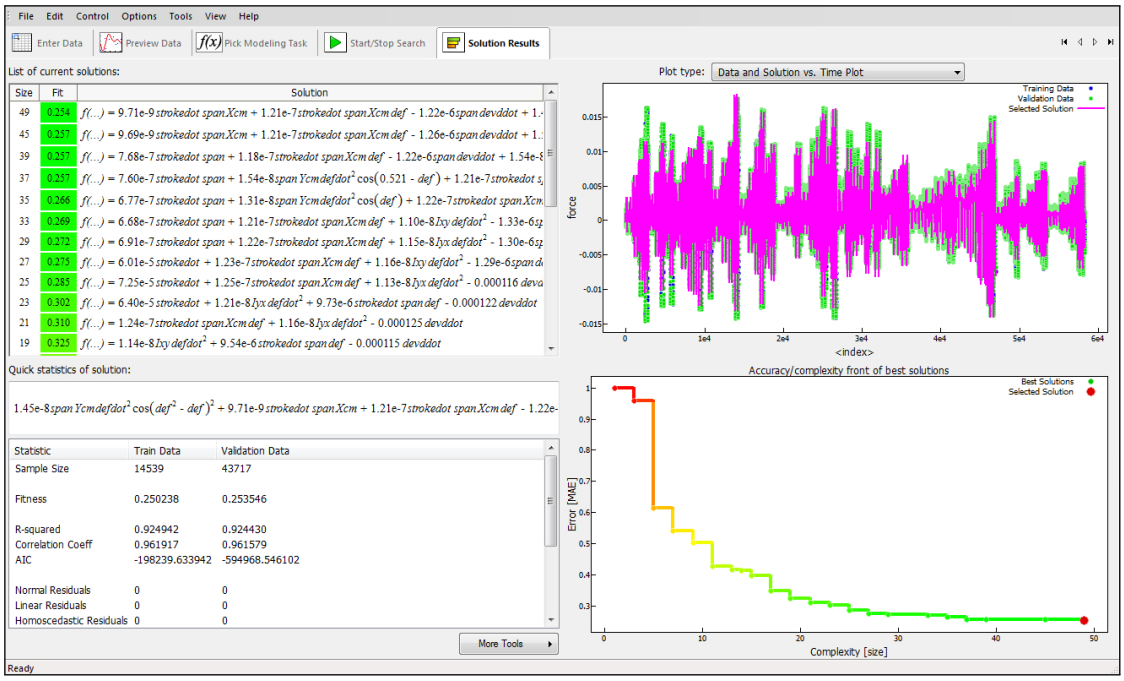

Figure 4.9: Screenshot of the software performing a model search on the experimental data. The screen contains a list of candidate models, a plot comparing one of the listed models to the data, an accuracy/complexity (Pareto) front showing all listed models and a calculation of solution statistics.

equations on 58 of the 68 total experiments simultaneously, with the remaining ten reserved for testing. These 58 sets of experimental data were contained within a single spreadsheet listing roughly two periods of smoothed, registered flapping data per experiment. The data consisted of instantaneous measured force along with the measured value of each kinematic variable, the first and second computed derivatives of those variables, and the geometric parameters necessary to describe the wing's shape and distribution of area, totaling 31 separate columns of data.

By training on 58 experiments simultaneously, Eureqa generated equations that fit all of the data, using the some, but not all, of the provided variables to

account for variations in kinematics and wing geometry between experiments. Table 4.3 lists six of the equations generated by Eureqa to describe the experimental force measurements. The duration of the Eureqa search that produced these results was approximately 24 hours and utilized 60 cores on a computing cluster running the Eureqa server application. Mean absolute error (MAE) was used as the fitness metric during the search.

Model	**Terms/Formula**	**Size**	**MAE**
U^2 Planar 1	$L_{planar}, F_{inertial\ (pendulum\ only)}$	32	1.23×10^{-3}
U^2 Planar 2	$L_{planar}, F_{inertial}$	46	1.06×10^{-3}
U^2 Total	$L_{trans}, F_{inertial}$	96	1.06×10^{-3}
Whitney-Wood	$L_{trans}, AM_{trans}, AM_{rot}$	121	9.21×10^{-4}
Pesavento-Wang	$L_{trans}, L_{rot}, AM_{trans}, AM_{trans,rot}$	130	9.01×10^{-4}
EQ_6	$C_1 RY_{CM}\dot{\psi}^2 + C_2 RX_{CM}\psi\dot{\phi} - C_3 R\ddot{\theta}$	12	8.08×10^{-4}
EQ_5	$C_1 RX_{CM}\psi\dot{\phi} - C_2 Rc_{trailing}\dot{\psi}^2 - C_3 R\ddot{\theta}$	13	8.08×10^{-4}
EQ_4	$C_1 RY_{CM}\dot{\psi}^2 \cos(\psi) + C_2 RX_{CM}\psi\dot{\phi} - C_3 R\ddot{\theta}$	14	7.97×10^{-4}
EQ_3	$C_1 RY_{CM}\dot{\psi}^2 \cos(\psi - \psi^2) + C_2 RX_{CM}\psi\dot{\phi} - C_3 R\ddot{\theta}$	16	7.83×10^{-4}
EQ_2	$C_1 RY_{CM}\dot{\psi}^2 \cos(\psi) + C_2 RX_{CM}\psi\dot{\phi} - C_3 R\dot{\phi}\psi\dot{\psi} - C_4 R\ddot{\theta}$	19	7.50×10^{-4}
EQ_1	$C_1 RY_{CM}\dot{\psi}^2 \cos(\psi) + C_2 RX_{CM}\psi\dot{\phi} - C_3 R\dot{\phi}\psi\ddot{\theta} - C_4 R\dot{\phi}\psi\dot{\psi} - C_5 R\ddot{\theta}$	24	7.15×10^{-4}

Table 4.3: Comparison of data-driven models and analytical equations of lift. The Eureqa models are sorted in ascending order of Akaike information criterion (AIC). The size of the equations is calculated as the sum of arithmetic and trigonometric operators required to compute a force prediction from kinematic and geometric data. The mean absolute error (MAE) reported is the average MAE from all ten test experiments after individually fitting all coefficients on each of the test experiments.

Fig. 4.10 shows the force predictions of four Eureqa models on the set of ten randomly selected experiments that were withheld from model training explicitly for computing the accuracy of these models. Most of the models vary only slightly from each other and show strong qualitative and quantitative agreement with the six experiments used for testing. In most cases, the Eureqa models reflect the subtle structure of peaks and troughs in the measured data, even if they do not match precisely. This result suggests that the underlying structure of these Eureqa models reflects the true physics and is not an artifact of

over-fitting, as these equations were never trained on these ten experiments.

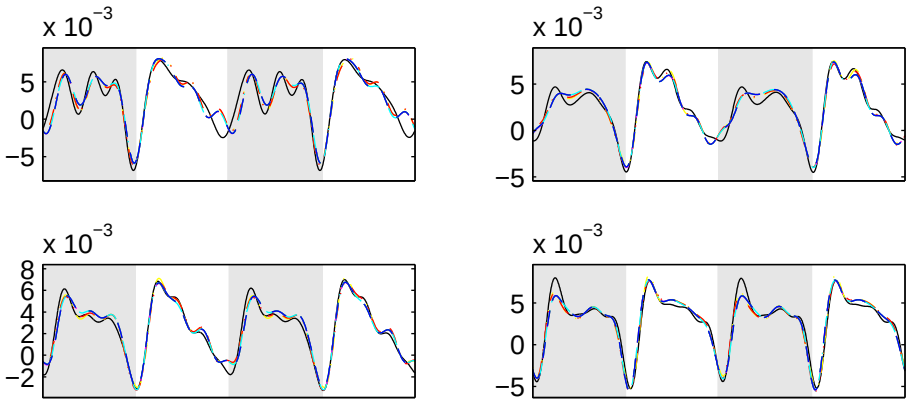

Figure 4.10: Force predictions of four models generated by Eureqa, compared to experimental measurements (black). Many of these equations show strong qualitative agreement with the subtle peaks and troughs in the experimental data, indicating structural validity of the equations rather than over-fitting since these experiments were reserved for testing and were not included in the training data for Eureqa.

4.4.1 Training on One Experiment vs. Many Experiments

It is possible to model single experiments using Eureqa with comparable equation size and accuracy to the models that were trained on all 58 training experiments simultaneously. However, training on a single set of experimental data highlights a major potential pitfall of data-driven modeling, as the resulting single-experiment equations are generally over-fit and do not generalize to other data exhibiting the same physical processes. For example, the following equation is one of many produced by Eureqa training on a single experiment:

$$\frac{\frac{C_1\psi\sin(\psi)}{C_2+\psi\ddot{\theta}\cos(\psi)\sin(\psi)+C_3\theta-C_4\psi-\phi} - C_5\dot{\theta} - C_6}{\cos(C_7+\dot{\theta})} \tag{4.9}$$

Fig. 4.11(a) shows the force prediction of this equation on the experiment on its training data while Fig. 4.11(b) and Fig. 4.11(c) show the force prediction on two of the experiments not used for training. While this equation matches its training data closely, it does not provide accurate predictions of the test experiments, suggesting that it is simply over-fitting the training data and failing to capture the underlying physical phenomena that should be observed in all data.

In contrast, Fig. 4.11(d), Fig. 4.11(e) and Fig. 4.11(f) show the force predictions of the EQ_1 model on the same experiments. This Eureqa model was trained on 58 experiments including the experiment used to train Equation 4.9, but was not trained on the experiment depicted in Fig. 4.11(e) and Fig. 4.11(f). Nevertheless, this Eureqa model provides predictions of data outside its training set that match the structure of peaks and troughs with strong quantitative accuracy.

Since Equation 4.9 is unable to accurately predict forces outside its training set, it is unlikely to offer any insight into the underlying physical processes governing the experimental measurement. EQ_1, however, must capture some of the underlying structure of the physics in order to generalize to data upon which it was not trained. In data-driven modeling, training on many experiments simultaneously helps to reject candidate equations that may fit some, but not all, of the data, and helps to retain those models that reflect the underlying physics and offer insight into the structure of the additive components that compose the observed behavior of a complex dynamical system.

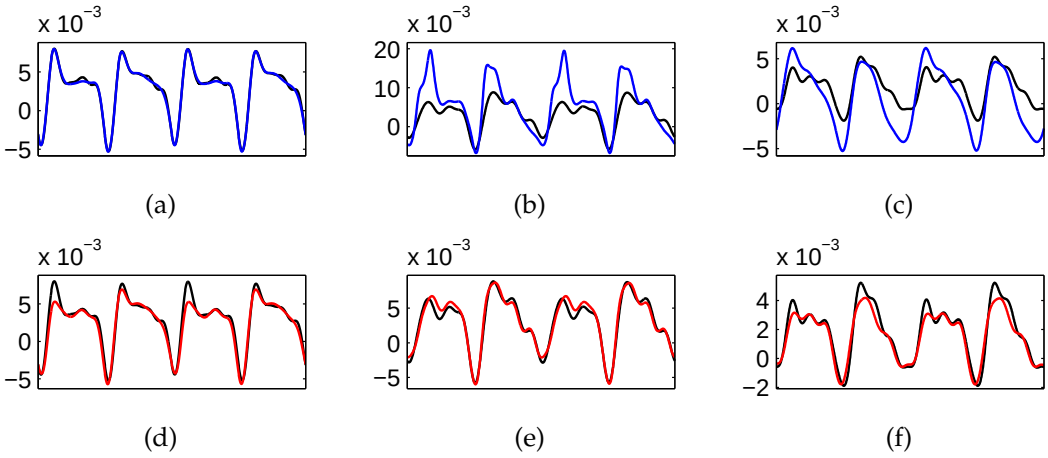

Figure 4.11: Force predictions of an equation that was trained on data from a single experiment (blue), compared to force predictions of EQ_1 (red), which was trained on the data from 58 experiments simultaneously. (a) and (d) show comparable performance of these two equations on data from their training set. However, (b) and (c) show that the equation trained on data from a single experiment fails to provide an accurate prediction of data outside its training set, whereas (e) and (f) show that EQ_1 provides a qualitatively and quantitatively accurate prediction of the same forces outside its training set.

4.4.2 Separation of Understandable Physical Effects

One powerful result of data-driven modeling is that in many cases, terms from the Eureqa models closely match physically understandable terms from the analytical models. Taking the Eureqa model EQ_4 as an example, all three terms show strong resemblance to inertial and aerodynamic components of the analytical models. Fig. 4.12 shows a comparison between the simple velocity-squared aerodynamic lift prediction and the second term of EQ_4: $C_2 R X_{CM} \psi \dot{\phi}$. These two calculations are numerically very similar, yet the third term of EQ_4 is much simpler than L_{trans}.

Similarly, the sum of terms 1 and 3, $C_1 R Y_{CM} \dot{\psi}^2 \cos(\psi) - C_3 R \ddot{\theta}$, closely approx-

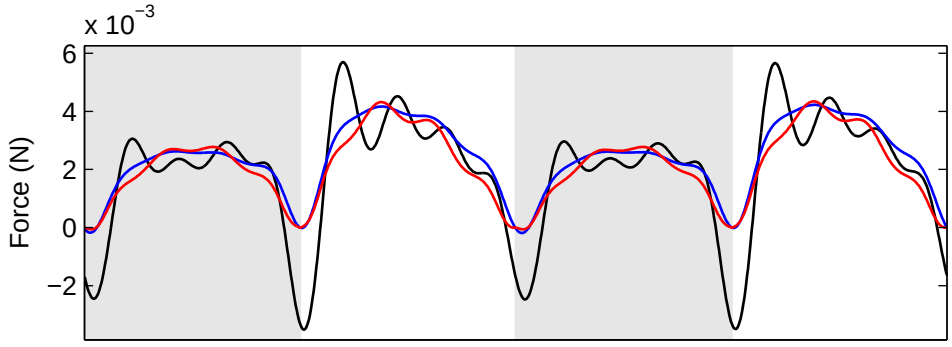

Figure 4.12: Primary translational aerodynamic lift based on a standard velocity-squared calculation used in analytical models (red) compared to one term of EQ_4 equation (blue) showing close agreement despite its significantly different form, with total force measurement (black) plotted for reference.

imates the calculation of inertial forces including the pendulum motion of the wing as well as the out-of-plane deviation. Fig. 4.13 shows these two calculations indicating very similar structure. While the EQ_4 approximation of these inertial forces does not precisely match the analytical calculation, it follows a very similar pattern and is much simpler. Remarkably, these inertial terms utilize some of the same variable combinations as the analytical calculations to express the inertial force, namely $\dot{\psi}^2 \cos(\psi)$ and $\ddot{\theta}$, with different coefficients to express the geometric variation between wings and a small angle approximation $cos(\theta) \approx 1$ for small out-of-plane deviation angles.

Table 4.4 lists a quantitative measurement of the fitness impact of each term in the model EQ_4. Eureqa calculates fitness impact of a term by replacing it with its mean value and measuring the decrease in fitness of the resulting equation. Thus, percentages do not add to 100% but rather the values give a relative measure of impact. The second term has the greatest impact on the fitness of EQ_4 because it corresponds to aerodynamic lift and accounts for a major part of the

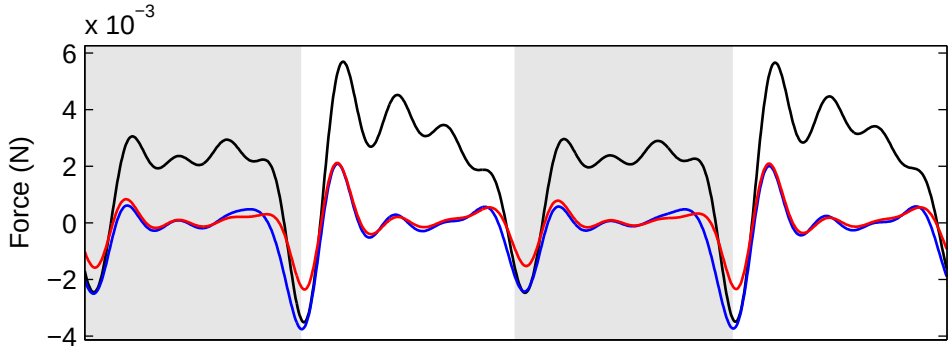

Figure 4.13: Comparison of inertial force calculations between the complete analytical model including pendulum motion and out-of-plane deviation (red) with the EQ_4 approximation (blue). The total measured force (black) is shown for reference.

shape of the force profile. The first term, representing a portion of the inertial effects, has less fitness impact but is significant nonetheless. The third term, representing forces resulting from out-of-plane deviation of the wing, has the smallest impact on the overall accuracy of the model. Equations EQ_1 and EQ_2 include additional terms with very small fitness impacts less than 5%, and serve as minor corrections associated with stroke reversal much like the added mass terms in the analytical models.

Term	**Fitness Impact**
$C_1 R Y_{CM} \dot{\psi}^2 \cos(\psi)$	-63.5%
$C_2 R X_{CM} \psi \dot{\phi}$	-197.4%
$C_3 R \ddot{\theta}$	-29.9%

Table 4.4: Statistics produced by Eureqa for the individual terms of the EQ_4 equation. The fitness impact is calculated by replacing the term with its mean value and measuring the change in fitness, therefore the percentages do not add to 100% but are intended to give a relative measure of impact.

In comparison with data-driven models trained on single experiments, which may contain large compound fractions, many nested trigonometric func-

tions, or other components that may be difficult to interpret, Eureqa models such as EQ_4 exhibit the profound behavior of separating distinct physical effects in a way that is understandable to the observer. In this case, the separation of aerodynamic lift from inertial forces suggests that these forces are not strongly coupled in the 58 sets of experimental training data, since no candidate models on the Pareto front convolved these effects. It is this separation of different physical effects into understandable components that suggests a data-mining approach could serve as a powerful tool in identifying the fundamental building blocks of many different complex dynamical systems.

4.5 Evaluation of Model Performance

An evaluation of model performance allows comparison between analytical models and the equations developed through the data mining process. Equations are judged by their accuracy and complexity, both of which can be measured in a variety of ways. In this case, the complexity or size of an equation was measured by simply counting the number of arithmetic and trigonometric operators used to combine the measured kinematic variables and geometric properties into an equation for force produced by a flapping wing. Both the Eureqa models and the analytical equations are measured in this way. For fairness, constants in the analytical models that would have been lumped together into larger coefficients by Eureqa (such as material density, air density, π or factors of integration) are also lumped together in the calculations of size for the analytical equations. The size of the inertial calculations was added to the sizes of analytical lift calculations. The pendulum motion has an equation size of 13 and the total inertial calculation including out-of-plane deviation has a size of 27.

Table 4.3 shows the size of all equations considered in this study, and indicates that the analytical models are all significantly more complex than the Eureqa models. One of the reasons for high complexity in the analytical models is the strict dependence on wing geometry and integration of forces over the span and chord of the wing. A second reason for the complexity in analytical models is the number of geometric and coordinate transformations required to compute the necessary linear and rotational velocities. In this sense, several terms used by Eureqa can be considered as approximations of much more subtle calculations of kinematic quantities.

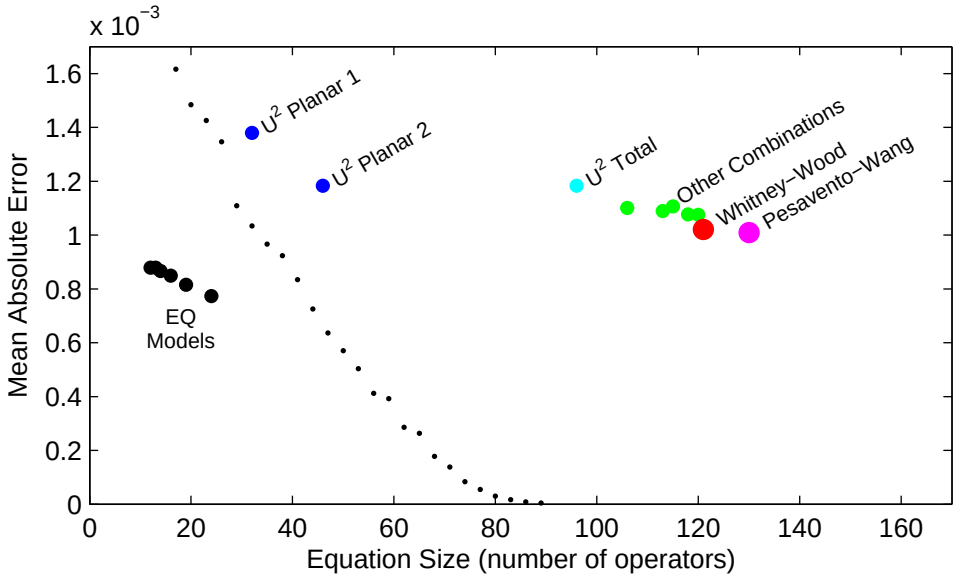

Figure 4.14: Pareto plot of all models with fitted coefficients, depicting accuracy as a function of model complexity. Eureqa equations are simultaneously more accurate and much simpler than analytical models.

The accuracy of each equation was measured as the mean absolute error (MAE). Fig. 4.14 shows the Pareto plot of all models considered, depicting accuracy as a function of model complexity. This plot reflects average model errors computed after fitting all coefficients to the data from the ten test experi-

ments. As a means of comparing the information content of an equation against a benchmark containing no information about the physical system, polynomials were fit to each of the ten test experiments over a range of exactly one wing stroke. The average MAE and equation size for these polynomials is shown by the black line, indicating that Eureqa models are simpler and more accurate than the polynomial while all analytical models are more complex or less accurate.

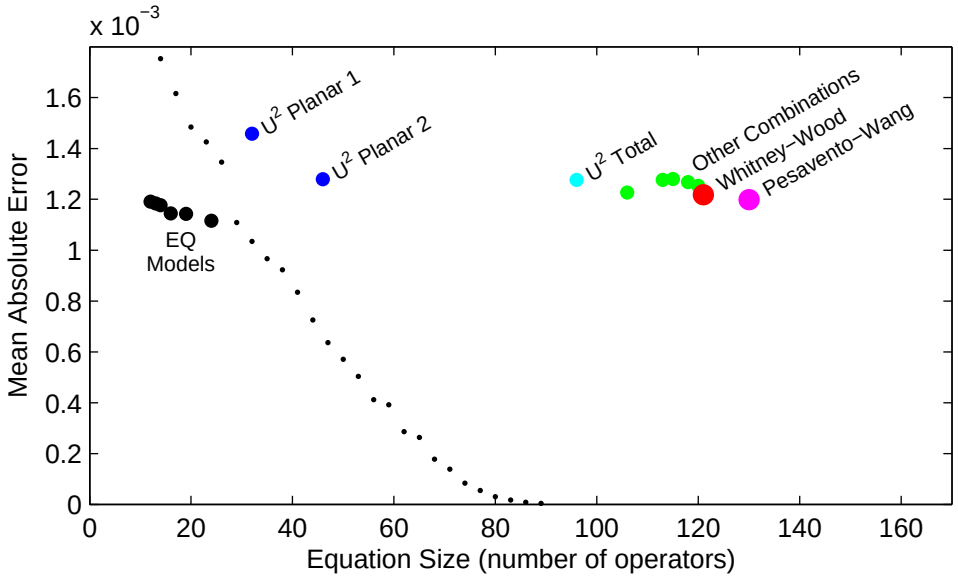

Figure 4.15: Pareto plot of all models using average or Eureqa-generated coefficients, demonstrating that the accuracy of Eureqa models is not overly dependent on coefficient fitting.

It is important to note that the Eureqa models were trained with MAE as their fitness function, however they could also be trained and evaluated using other fitness metrics. Furthermore, all Eureqa models have between three and five coefficients, so tuning these coefficients allows further minimization of error compared to the analytical models, which have between one and three. Nevertheless, discovery of models with smaller error than theoretical predictions that are simultaneously much simpler is a significant feat for the data mining pro-

cess and the algorithm behind the Eureqa software. Finally, Fig. 4.15 shows the Pareto plot of all models using the coefficients given by Eureqa for Eureqa equations and mean coefficient values from all 68 experiments for the analytical equations. This plot is very similar in its structure to the Pareto plot with fitted coefficients, indicating that Eureqa models and analytical equations have similar sensitivities to coefficient fitting, and that the Eureqa models do not depend heavily on coefficient fitting to achieve accuracy. This result further validates the information content of the data-driven models as a true reflection of the physical process that captures the effects of the salient variables.

CHAPTER 5

CONCLUSIONS

This research has demonstrated a variety of concepts and resulted in the development of new tools and methods for the study of insect flight and ornithopter design. The first-ever 3D printed ornithopter was designed, built and flown, demonstrating the viability of the use of 3D printing to create functional flapping wings with complex yet highly tuneable flexibility and dynamic behaviors. Not only was this the first 3D printed ornithopter, but it was nearly the lightest hovering ornithopter ever built, justifying the use of 3D printed materials for flight vehicles where lightweight materials are critical. Second, an experimental apparatus was developed to accurately measure the instantaneous lift forces produced by an at-scale flapping wing in air. Since most experimentation of aerodynamics at low and intermediate Reynolds numbers has been conducted in a liquid fluid such as oil or water, measurement of lift in air was a significant challenge and accomplishment. Finally, evaluations of aerodynamic models were made on flapping wings in air. Some of these models were developed from experiments in a liquid fluid or were based on 2D planar flow and other simplifying assumptions. The work presented in this thesis quantifies the performance of these models on flapping wings under the same conditions that they would be used in real ornithopters. The strong agreement between analytical models and the experimental measurements suggests that any three dimensional phenomena or unsteady effects are minor compared to the overall structure of the quasi-steady approximation.

One major unique thrust of this work was to apply a data-driven approach to modeling the forces on a flapping wing. The symbolic equations produced by

Eureqa were shown to be more accurate than any of the analytical models and were much simpler, in some cases by an order of magnitude in equation size. Furthermore, by dissecting these equations and examining individual terms, it was observed that Eureqa separated the measured forces into understandable physical effects. A lift term was found that was numerically similar to the standard translational lift, and an inertial term was found that was numerically similar to the complete calculation of the pendulum and out-of-plane motions with some analytical terms in common. Finally, by training Eureqa models on experimental data from 58 individual wing-amplitude-speed combinations simultaneously, Eureqa was able to separate distinct physical effects into additive terms rather than proposing large, inseparable formulas.

This application of a data-driven symbolic modeling approach suggests that Eureqa could be useful in phenomenological modeling of a wide variety of complex systems. Its ability to automatically identify distinct physical effects from large volumes of data makes it a powerful tool for identifying the structure of contributions from building blocks that make up the complete observed behavior of a dynamical system.

5.1 Contributions of This Thesis

1. A method of 3D printing flapping wings was developed. Wings were composed of a wing surface film as thin as 32 μm and a flexible structure that was designed to deflect to an appropriate angle of attack during flapping.
2. A complete passively stable hovering ornithopter was designed, built and flown using 3D printed wings and a 3D printed structure. Weighing 3.89

grams, this ornithopter was one of the lightest ever flown.

3. An experimental apparatus was developed to measure the instantaneous forces on a wing flapping in air while capturing the kinematics through a high speed camera and accompanying custom-written MATLAB code.
4. Analytical models from the literature were compared to the measured lift forces and evaluated according to their accuracy and equation size.
5. Symbolic equations were developed using a data mining approach enabled by the Eureqa software to describe the experimentally measured forces produced by a flapping wing. These equations were more accurate than the analytical models and were much simpler, while lending insight by separating the total force prediction into a sum of distinct, physically understandable effects.

APPENDIX A

MOTION TRACKING CODE

```
%% Motion Tracking Code for Rectangular 3D Printed Wings
function [] = fnvideo(folderName,vidName,cameraSpeed,vidStartFrame)

% FNVIDEO video processing.
%   FNVIDEO is a function that loads a high speed video of a flapping wing,
%   filmed as documented in this thesis, and extracts the 3D kinematics of
%   the flapping motion.
%
%   'folderName'        File location of the video and supporting files.
%   'vidName'           File name of video.
%   'cameraSpeed'       Either 420 or 210 (frames per second).
%   'vidStartFrame'     Frame number to begin processing, allows skipping
%                       large portions of unnecessary video.
%
%   SUPPORTING FILE:    'constants.mat' stores the geometric variables
%                       needed to describe the shape of the wing for size
%                       calibration in the video frame.
%
%   OUTPUT FILE:        'video.mat' stores the stroke and deflection angles
%                       of the wing for every wing frame, along with the
%                       vertical coordinates of the center of area of the
%                       wing and the vertical coordinates of the leading-
%                       and trailing-edge corners of the wingtip, which are
%                       needed for computing the out-of-plane deviation
%                       angle of the wing.

%% Import Wing Geometry and Set Controls
load ([folderName 'constants.mat']);    % Load geometric wing constants
chord = chordLower+chordUpper;          % Compute total wing chord length
nLines = 5;                             % Number of Hough lines to use in
                                        % obtaining stroke angle
%% Select Camera Speed, Set Pixel Regions and Calibrate Distances
switch cameraSpeed
    case 420    % 420 Frames per second, lower spacial resolution
        ytd = 10:120; xtd = 10:178;     % Top-down region
        ys = 50:112; xs = 192:224;      % Side view region
        pxconvert = 48.7622/100;        % Top-down distance calibration
        pxconvertside = 35.5815/100;    % Side view distance calibration
    case 210    % 210 Frames per second, greater spacial resolution
        ytd = 36:254; xtd = 10:378;     % Top-down region
        ys = 110:234; xs = 408:480;     % Side view region
        pxconvert =   103.0409/100;     % Top-down distance calibration
        pxconvertside = 75.1884/100;    % Side view distance calibration
end

%% Geometry
spanpx = span*pxconvert;                % Wingspan in pixels
chordpx = chord*pxconvert;              % Chord length in pixels
areapx = spanpx*chordpx-spanpx*1.8*pxconvert; % Wing area in pixels
```

```
%% Read in Video
movobj = mmreader([folderName vidName]);get(movobj);        % Read in video
nFrames = movobj.NumberOfFrames;        % Obtain number of frames

%% Initialize Kinematic Variables (multiple for redundant calculations)
stroke_beam = nan(nFrames,nLines); stroke = nan(nFrames,1); % Stroke
def = zeros(nFrames,1);                 % Deflection
cm_height = zeros(nFrames,1);           % Vertical motion of center of area
xcorners = nan(nFrames,2);              % Vertical motion of wingtip

%% For Each Video Frame, Extract Kinematic Variables
range = vidStartFrame:nFrames;
for n = range
    % Read in movie frame, isolate top-down view and conver to binary image
    mov = read(movobj,n);               % Read in movie frame
    Itd = mov(ytd,xtd,:);               % Isolate top-down view region
    Itdgray = rgb2gray(Itd);            % Convert to grayscale
    level1 = graythresh(Itdgray);       % Compute binary threshold
    Itdbw = im2bw(Itdgray,level1);      % Convert top-down to binary image
    Itdbw = bwareaopen(Itdbw,10);       % Remove objects of <10 px
    cm1 = regionprops(Itdbw,'centroid');% Find center of area

    % Use color to find the main beam
    redness = Itd(:,:,1)-Itd(:,:,2);    % Compute "redness" of each pixel
    [Ifind,Jfind,Vfind] = find(redness);% Find non-zero values of redness
    [~,Isort] = sort(Vfind,'descend');  % Sort red pixels by redness value
    npts = 1000;                        % Number of red points to use
    Itdrgbbeam = zeros(size(redness));  % Allocate blank frame for red beam
    Itdrgbbeam(sub2ind(size(Itdrgbbeam),Ifind(Isort(1:npts)),...
        Jfind(Isort(1:npts)))) = 1;     % Add reddest points to blank frame
    Itdrgbbeam = bwmorph(Itdrgbbeam,'thin',2);  % Thin the beam to a line

    % Hough transform to fit lines to represent the main beam
    xy = cell(nLines,1);                % Initialize main beam endpoints
    lrsignholder = nan(1,nLines);       % Sign of deflection angle
    [H,T,R] = hough(Itdrgbbeam,'Theta',-60:.2:60);  % Hough transform
    P = houghpeaks(H,nLines);           % Find peaks in Hough space
    lines = houghlines(Itdrgbbeam,T,R,P,...
        'MinLength',100,'FillGap',60);  % Create lines from P peaks

    % Extract stroke angle and sign of deflection angle from lines
    for i = 1:length(lines)
        if isfield(lines(i),'point1')   % If Hough found a line, then...
        stroke_beam(n,i) = lines(i).theta; % Store angle of line
        xy{i} = [lines(i).point1; lines(i).point2]; % Unpack line endpoints
        [~,Ixy] = sort(xy{i});...
            xy{i} = xy{i}(Ixy(:,2),:);  % Sort endpoints by y-coordinate
        lrsignholder(i) = sign(det([xy{i}(2,:)-xy{i}(1,:);...
            cm1(1).Centroid-xy{i}(1,:)])); % Sign of deflection angle
        end
    end
    lrsign = sign(mean(lrsignholder(~isnan(lrsignholder)))); % Mean sign
    stroke(n) = mean(stroke_beam(n,~isnan(stroke_beam(n,:)))); % Mean angle
```

```
    % Compute projected wing area to obtain deflection angle
    areameas = bwarea(Itdbw)-cArea;     % Measured area
    def(n) = lrsign*asind(areameas/areapx); % Calibrated deflection angle

    % Side view to obtain vertical (out-of-plane) wing motion
    Is = mov(ys,xs,:);                  % Isolate side view region
    Isgray = rgb2gray(Is);              % Convert to grayscale
    level2 = graythresh(Isgray);        % Compute threshold for BW
    Isbw = im2bw(Isgray,.8*level2);     % BW image
    Isbw = bwareaopen(Isbw,10);         % Remove objects of <10 px
    Isbw = imclose(Isbw,strel('disk',2)); % Morphologically close image
    cm2 = regionprops(Isbw,'centroid'); % Compute location of CM
    cm_height(n) = cm2(1).Centroid(1)/pxconvertside; % Compute height of CM

    % Edge of wing in side view for identifying wingtip corners
    Isedge = edge(Isbw);                % Edge of wing image
    [yedge,xedge] = ind2sub(size(Isbw),find(Isedge)); % List of edge points
    edgepts = [yedge,xedge];            % Edge points in array subscripts
    edgepts = edgepts(edgepts(:,1)<cm2(1).Centroid(2),:); % +y from CM
    ledgepts = edgepts(edgepts(:,2)<cm2(1).Centroid(1),:); % left of CM
    redgepts = edgepts(edgepts(:,2)>cm2(1).Centroid(1),:); % right of CM

    % Distances from leading and trailing edge points to wing center
    lxdistfromcenter = (cm2(1).Centroid(1)-ledgepts(:,2)).^2;
    rxdistfromcenter = (cm2(1).Centroid(1)-redgepts(:,2)).^2;
    lydistfromcenter = (cm2(1).Centroid(2)-ledgepts(:,1)).^2;
    rydistfromcenter = (cm2(1).Centroid(2)-redgepts(:,1)).^2;

    % Pick points to represent the leading and trailing edge wing corners
    nspts = 10;                         % Number of points to use
    [~,bi] = sort(10./lxdistfromcenter+1./lydistfromcenter,'ascend');
    if size(ledgepts,1) >= nspts,bottompts = [ledgepts(bi(1:nspts),2)...
        ledgepts(bi(1:nspts),1)];end    % Store leading edge corner points
    [~,ti] = sort(10./rxdistfromcenter+1./rydistfromcenter,'ascend');
    if size(redgepts,1) >= nspts,toppts = [redgepts(ti(1:nspts),2)...
        redgepts(ti(1:nspts),1)];end    % Store traling edge corner points

    % Vertical heights of wing corners in mm, mean of corner points
    xcorners(n,:) = [mean(bottompts(:,1)) mean(toppts(:,1))]/pxconvertside;
end

%% Package and Export Data
stroke = deg2rad(stroke);def = deg2rad(real(def)); % Convert to radians
save([folderName 'video.mat'],'stroke','def','cm_height','xcorners')
end
```

APPENDIX B

ORNITHOPTER IMAGES

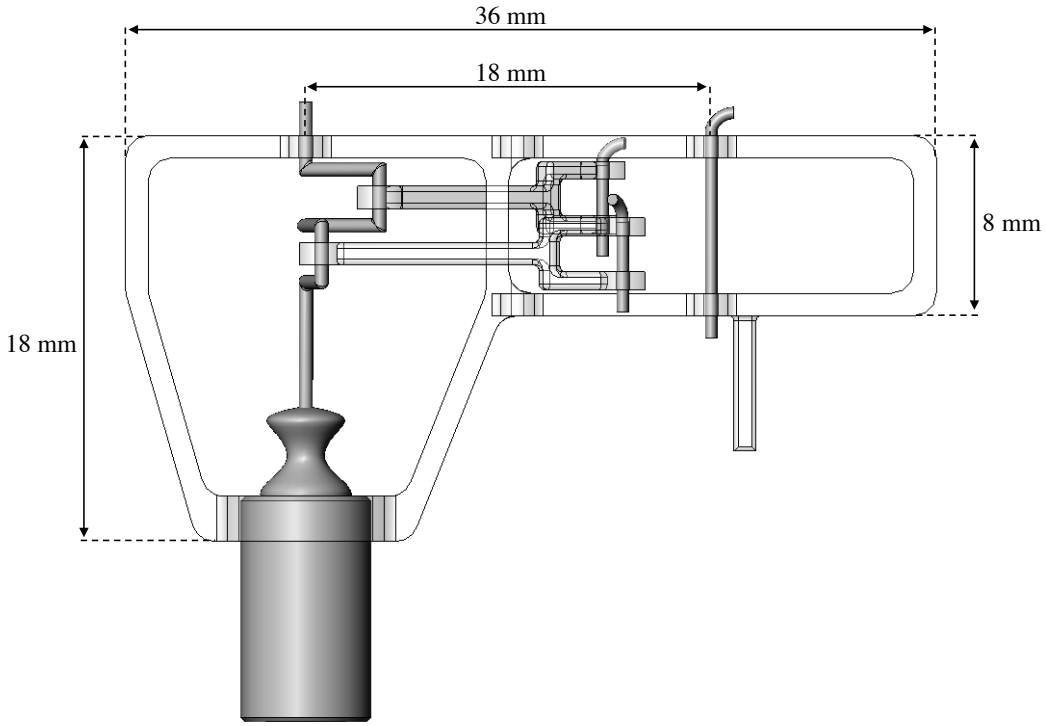

Figure B.1: Dimensions of ornithopter fuselage.

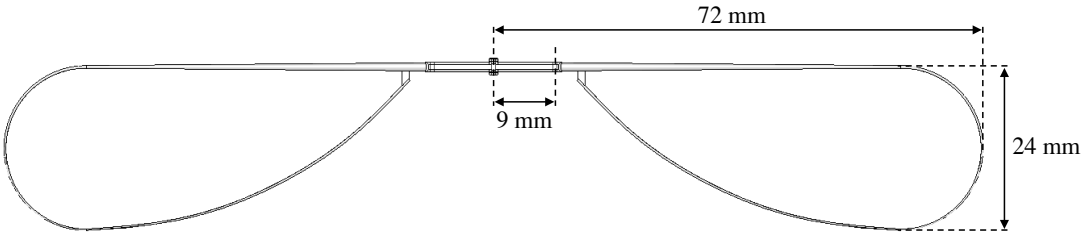

Figure B.2: Dimensions of ornithopter wing.

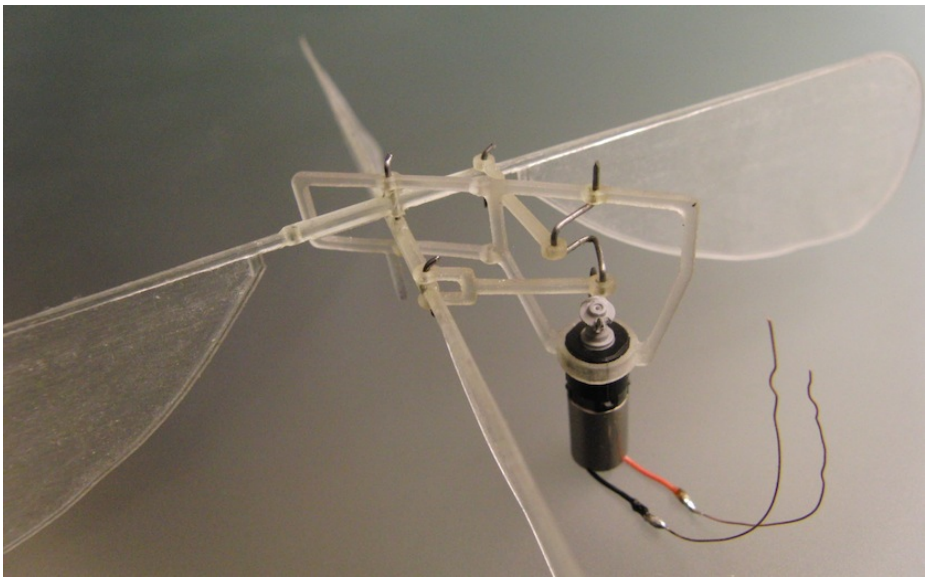

Figure B.3: Ornithopter showing motor, offset crank, connecting rods and hinge pins.

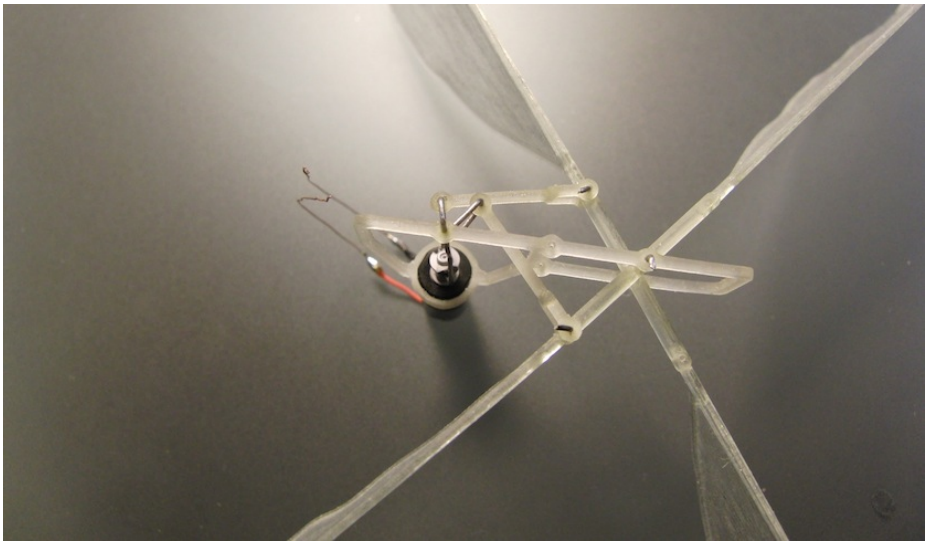

Figure B.4: Ornithopter showing geometry of the wing-driving mechanism and offset crank.

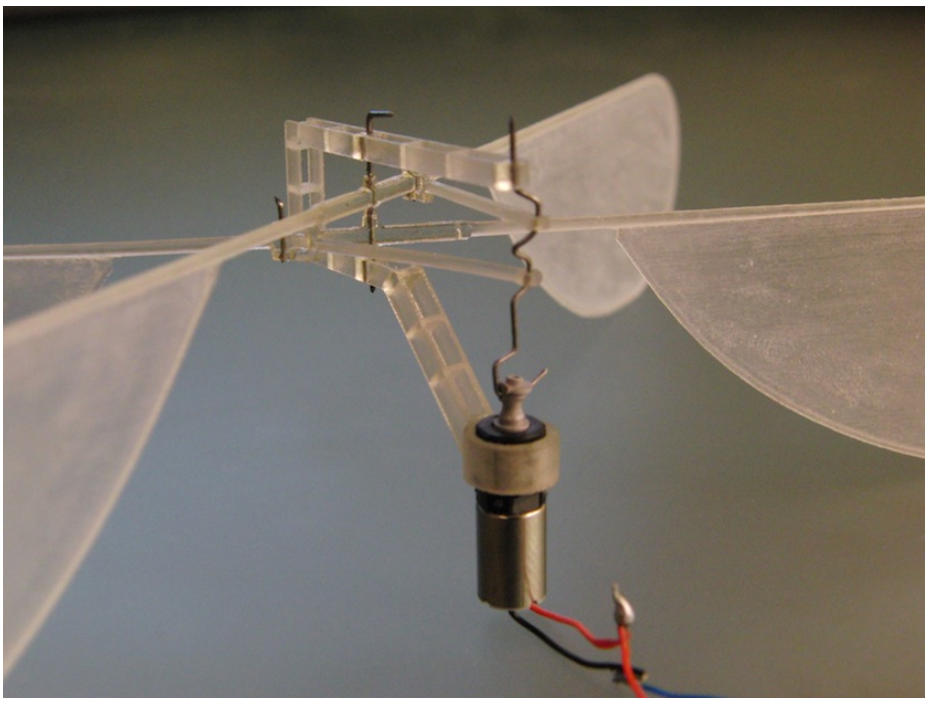

Figure B.5: Ornithopter prototype used in tethered flight tests.

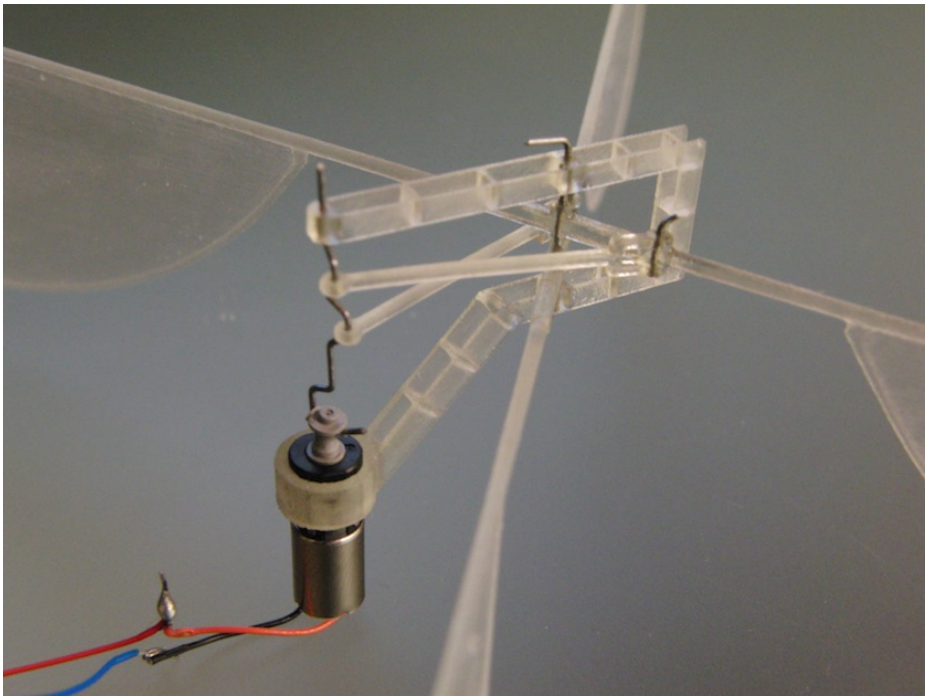

Figure B.6: Ornithopter prototype used in tethered flight tests.

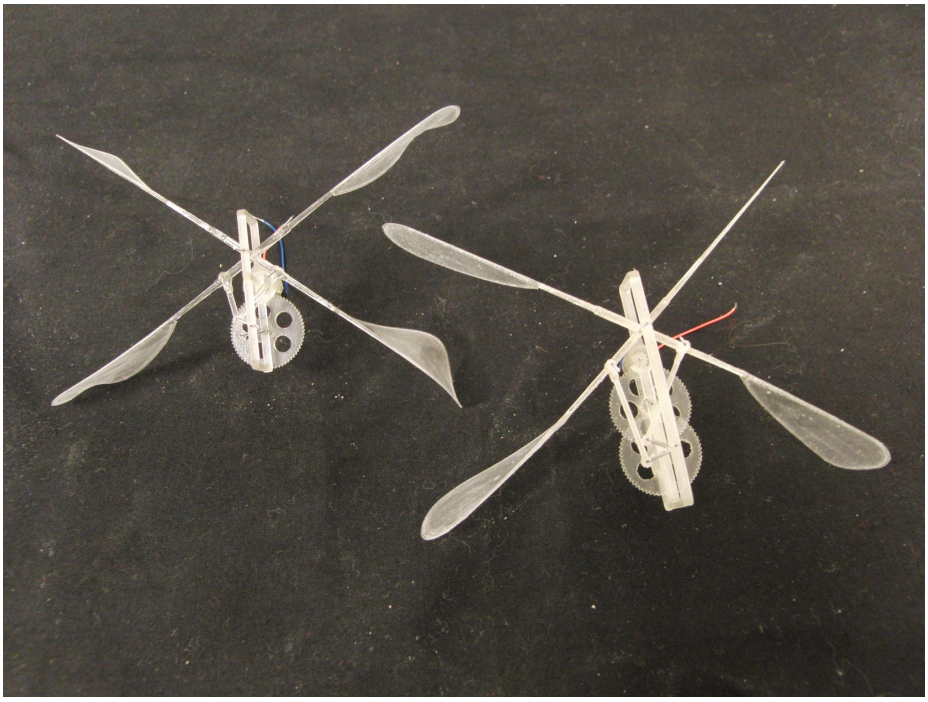

Figure B.7: Prototypes for future smaller ornithopter designs.

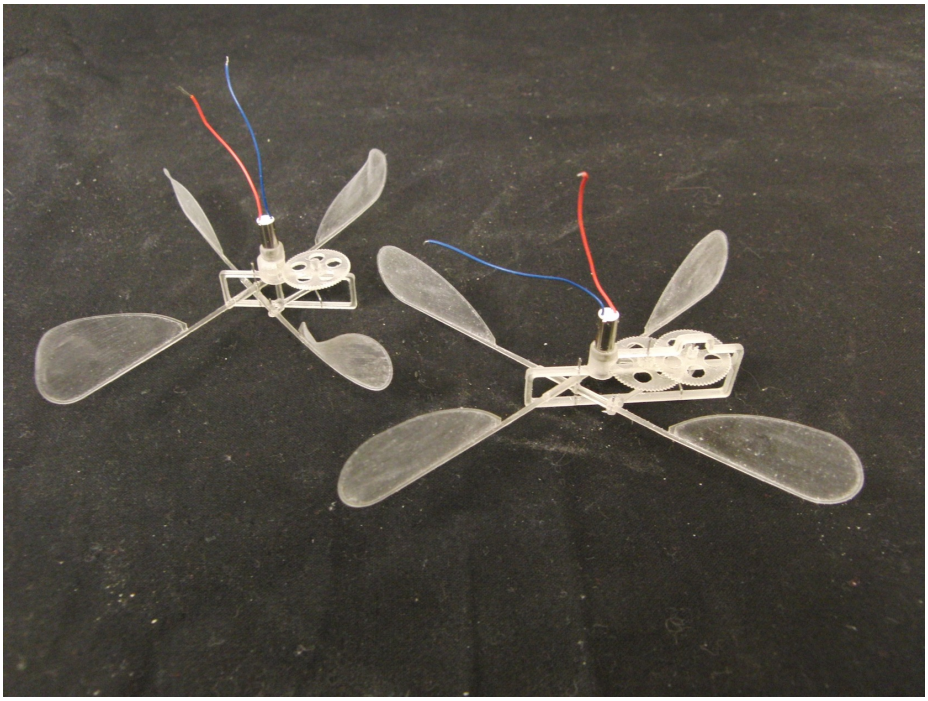

Figure B.8: 3D printed gears and driving mechanisms used in ornithopter prototypes.

Figure B.9: Ornithopter taking flight and hovering.

BIBLIOGRAPHY

[1] AeroVironment. Darpa awards aerovironment phase ii contract extension for nano air vehicle development program [online]. Accessed 4/9/10. http://www.avinc.com/downloads/NAVPRLongDARPAV4.doc.pdf, 2009.

[2] A. Andersen, U. Pesavento, and Z. J. Wang. Analysis of transitions between fluttering, tumbling and steady descent of falling cards. *Journal of Fluid Mechanics*, 541:91–104, 2005.

[3] A. Andersen, U. Pesavento, and Z. J. Wang. Unsteady aerodynamics of fluttering and tumbling plates. *Journal of Fluid Mechanics*, 541:65–90, 2005.

[4] E. Bautu, A. Bautu, and H. Luchian. Symbolic regression on noisy data with genetic and gene expression programming. In *SYNASC'05*, pages 321–324, 2005.

[5] A. J. Bergou, L. Ristroph, J. Guckenheimer, I. Cohen, and Z. J. Wang. Fruit flies modulate passive wing pitching to generate in-flight turns. *Phys. Rev. Lett.*, 104(14):148101, Apr 2010.

[6] A. J. Bergou, S. Xu, and Z. J. Wang. Passive wing pitch reversal in insect flight. *J. Fluid Mech.*, 591:321–337, 2007.

[7] J. Bongard and H. Lipson. Automated reverse engineering of nonlinear dynamical systems. *Proceedings of the National Academy of Sciences*, 104(24):9943–9948, 2007.

[8] N. Chronister. Micro air vehicle ornithopters [online]. Accessed 4/9/10. http://www.ornithopter.org/history.mav.shtml, 2010.

[9] G. C. H. E. de Croon, K. M. E. de Clerg, R. Ruijsink, B. Remes, and C. de Wagter. Design, aerodynamics, and vision-based control of the delfly. *Int. J. of Micro Air Vehicles*, 1(2):71–97, 2009.

[10] DelFly. Accessed 4/9/10. http://www.delfly.nl/, 2010.

[11] M. H. Dickinson, F. Lehmann, and S. P. Sane. Wing rotation and the aerodynamic basis of insect flight. *Science*, 284:1954–1960, 1999.

[12] W. B. Dickson, P. Polidoro, M. M. Tanner, and M. H. Dickinson. A linear systems analysis of the yaw dynamics of a dynamically scaled insect model. *Journal of Experimental Biology*, 213(17):3047–3061, 2010.

[13] J. Duffy and J. Engle-Warnick. *Using Symbolic Regression to Infer Strategies from Experimental Data*, pages 61–82. Physica-Verlag, 2002.

[14] C. P. Ellington. The aerodynamics of hovering insect flight. i. the quasi-steady analysis. *Philosophical Transactions of the Royal Society of London. B, Biological Sciences*, 305(1122):1–15, 1984.

[15] C. P. Ellington. The novel aerodynamics of insect flight: Applications to micro-air vehicles. *J. Exp. Biol.*, 202(23):3439–3448, 1999.

[16] A. R. Ennos. The inertial cause of wing rotation in diptera. *Journal of Experimental Biology*, 140(1):161–169, 1988.

[17] C. Fillon and A. Bartoli. Symbolic regression of discontinuous and multivariate functions by hyper-volume error separation (hves). In *Evolutionary Computation, 2007. CEC 2007. IEEE Congress on*, pages 23 –30, sept. 2007.

[18] D. Floreano, J. C. Zufferey, M.V. Srinivasan, and C. Ellington, editors. *Flying Insects and Robots*. Springer, 2010.

[19] S. Forrest. Genetic algorithms: principles of natural selection applied to computation. *Science*, 261(5123):872–878, 1993.

[20] S. N. Fry, R. Sayaman, and M. H. Dickinson. The aerodynamics of free-flight maneuvers in drosophila. *Science*, 300(5618):495–498, 2003.

[21] C. Graetzel, S. Fry, F. Beyeler, Y. Sun, and B. Nelson. Real-time microforce sensors and high speed vision system for insect flight control analysis. In Oussama Khatib, Vijay Kumar, and Daniela Rus, editors, *Experimental Robotics*, volume 39 of *Springer Tracts in Advanced Robotics*, pages 451–460. Springer Berlin / Heidelberg, 2008.

[22] M. Karpelson, G. Y. Wei, and R. J. Wood. A review of actuation and power electronics options for flapping-wing robotic insects. In *IEEE International Conference on Robotics and Automation*, 2008.

[23] J. R. Koza, editor. *Genetic Programming: On the Programming of Computers by Means of Natural Selection*. MIT Press, 1992.

[24] F. Lehmann, S. P. Sane, and M. Dickinson. The aerodynamic effects of wing-wing interaction in flapping insect wings. *J. Exp. Biol.*, 208:3075–3092, 2005.

[25] R. Michelson and M. Naqvi. Extraterrestrial flight. In *Proc. von Karman Institute for Fluid Dynamics RTO/AVT Lecture Series on Low ReynoldsNumber Aerodynamics*, Brussels, Belgium, 2003.

[26] U. Pesavento and Z. J. Wang. Falling paper: Navier-stokes solutions, model of fluid forces, and center of mass elevation. *Phys. Rev. Lett.*, 93(14):144501, Sep 2004.

[27] U. Pesavento and Z. J. Wang. Flapping wing flight can save aerodynamic power compared to steady flight. *Phys. Rev. Lett.*, 103(11):118102, Sep 2009.

[28] W. Regan, F. van Breugel, and H. Lipson. Towards Evolvable Hovering Flight on a Physical Ornithopter. In *Artificial Life X : Proceedings of the Tenth International Conference on the Simulation and Synthesis of Living Systems*, pages 241–247. International Society for Artificial Life, The MIT Press (Bradford Books), 2006.

[29] C. Richter and H. Lipson. Untethered hovering flapping flight of a 3d-printed mechanical insect. *Artificial Life*, 17(2):73–86, 2011.

[30] L. Ristroph, A. J. Bergou, J. Guckenheimer, Z. J. Wang, and I. Cohen. Paddling mode of forward flight in insects. *Phys. Rev. Lett.*, 106(17):178103, Apr 2011.

[31] L. Ristroph, A. J. Bergou, G. Ristroph, K. Coumes, G. J. Berman, J. Guckenheimer, Z. J. Wang, and I. Cohen. Discovering the flight autostabilizer of fruit flies by inducing aerial stumbles. *Proceedings of the National Academy of Sciences*, 107(11):4820–4824, 2010.

[32] L. Ristroph, G. J. Berman, A. J. Bergou, Z. J. Wang, and I. Cohen. Automated hull reconstruction motion tracking (hrmt) applied to sideways maneuvers of free-flying insects. *J. Exp. Biol.*, 212:1324–1335, 2009.

[33] S. P. Sane and M. H. Dickinson. The aerodynamic effects of wing rotation and a revised quasi-steady model of flapping flight. *Journal of Experimental Biology*, 205(8):1087–1096, 2002.

[34] M. Schmidt and H. Lipson. Distilling free-form natural laws from experimental data. *Science*, 324(5923):81–85, 2009.

[35] M. Schmidt and H. Lipson. Solving iterated functions using genetic programming. In *Proceedings of the 11th Annual Conference Companion on Genetic*

and Evolutionary Computation Conference: Late Breaking Papers, GECCO '09, pages 2149–2154, New York, NY, USA, 2009. ACM.

[36] M. Schmidt and H. Lipson. Symbolic regression of implicit equations. In Rick L. Riolo, Una-May O'Reilly, and Trent McConaghy, editors, *Genetic Programming Theory and Practice VII*, Genetic and Evolutionary Computation, chapter 5, pages 73–85. Springer, Ann Arbor, 2009.

[37] L. I. Sedov. *Two-dimensional problems in hydrodynamics and aerodynamics*. Interscience, New York, 1st edition, 1965.

[38] M. Sun and Y. Xiong. Dynamic flight stability of a hovering bumblebee. *J. Exp. Biol.*, 208:447–459, 2005.

[39] G. K. Taylor and A. L. R. Thomas. Dynamic flight stability in the desert locust schistocerca gregaria. *J. Exp. Biol.*, 206:2803–2829, 2003.

[40] F. van Breugel, W. Regan, and H. Lipson. From insects to machines: A passively stable, untethered flapping-hovering micro air vehicle. *IEEE Robotics and Automation Magazine*, 15:68–74, 2008.

[41] S. M. Walker, A. L. R. Thomas, and G. K. Taylor. Photogrammetric reconstruction of high-resolution surface topographies and deformable wing kinematics of tethered locusts and free-flying hoverflies. *Journal of The Royal Society Interface*, 6(33):351–366, 2009.

[42] Z. J. Wang. Two dimensional mechanism for insect hovering. *Phys. Rev. Lett.*, 85(10):2216–2219, Sep 2000.

[43] Z. J. Wang. Dissecting insect flight. *Annu. Rev. Fluid Mech.*, 37:183–210, 2005.

[44] Z. J. Wang, J. M. Birch, and M. H. Dickinson. Unsteady forces and flows in low reynolds number hovering flight: two-dimensional computations vs robotic wing experiments. *Journal of Experimental Biology*, 207(3):449–460, 2004.

[45] J. P. Whitney and R. J. Wood. Aeromechanics of passive rotation in flapping flight. *Journal of Fluid Mechanics*, 660:197–220, 2010.

[46] R. J. Wood. The first takeoff of a biologically-inspired at- scale robotic insect. *IEEE Trans. on Robotics*, 24:341–347, 2008.

[47] M. I. Woods, J. F. Henderson, and G. D. Lock. Energy requirements for the flight of micro air vehiles. *Aeronautical Journal*, 105(1045):135–149, 2001.

[48] J. H. Wu and M. Sun. Unsteady aerodynamic forces of a flapping wing. *Journal of Experimental Biology*, 207(7):1137–1150, 2004.

[49] J. Young, S. M. Walker, R. J. Bomphrey, G. K. Taylor, and A. L. R. Thomas. Details of insect wing design and deformation enhance aerodynamic function and flight efficiency. *Science*, 325(5947):1549–1552, 2009.

[50] P. et al. Zdunich. Development and testing of the mentor flapping-wing micro air vehicle. *Journal of Aircraft*, 44:1701–1711, 2007.